

---

# CHAPTER **IV** NUMERICAL INVESTIGATIONS OF REINFORCED SOIL STRUCTURES

---

## **4.1 GENERAL**

---

In the preceding chapter, Chapter III, existing methodologies (RPFEM and LEFEM) based on plasticity and linear elastic theories have been reviewed and a new formulation to model the reinforced soil system is derived. Finally, the newly introduced formulations of the reinforced soil system have been incorporated into these numerical methods. In this chapter, the capability of the proposed methodology will be numerically investigated through some typical reinforced soil engineering problems, e.g. bearing capacity problems, slope stability problems, etc. It will be further illustrated that the methodology can solve an indeterminate axial force and shear force (/bending moment) distributions acting along the reinforcing members together with the load factor (a safety factor of the applied force) and velocity field of soils at limiting equilibrium state, simultaneously. As already explained in the previous chapter that nothing has been assumed in advance of the analysis unlike the conventional limiting equilibrium methods.

The general tendency of the solutions presented in this chapter is expected to provide enough confidence for the practicing engineers in order to make up their engineering judgment whether the method is applicable to daily design works or not. The example problems discussed in the present study are aimed at this purpose.

## 4.2 BEARING CAPACITY PROBLEMS

---

### 4.2.1 General

The first problem taken is a bearing capacity problem of a long shallow foundation idealized as a typical plane strain problem. The soil deposit beneath the footing is reinforced by a reinforcing material (e.g. geotextile /steel). For simplicity, first homogeneous clay under undrained condition (Mises material) is considered, and then another clay is considered whose undrained shear strength linearly increases along the depth. Due to symmetry of the foundation along the centerline, only right half of the soil mass is discretized by putting roller along the centerline (Fig. 4.1). All displacement boundary conditions are either roller or fixed support types. Flexible loading, rigid-smooth and rigid-rough footings are separately discussed.

A single reinforcing member is placed at different elevations in order to search an optimum position of the reinforcement where the maximum ultimate bearing capacity,  $Q_f$  can be obtained. The ultimate bearing capacity,  $Q_f$  is computed and also the initial footing loading~settlement relations are studied, employing the methodology proposed in the previous chapter, Chap. III (RPFEM and LEFEM). The corresponding computed tensile force distributions along the reinforcement; nodal velocity vectors are illustrated for each case dealt. Such figures demonstrate the effect of reinforcements at the limit equilibrium state of the soil mass. Detailed explanation is presented in the following paragraphs for each cases dealt separately.

### 4.2.2 Homogeneous Clay

The soil mass is assumed to be homogeneous clay with  $c_u=9.8$  kPa as undrained shear strength. The thickness of the clay deposit is 20 m and the width is 30 m. The width of the footing is equal to the depth of the clay ( $H=B(=2b)=20$ m). Thus, the foundation rock beneath the soil has no direct influence over the failure mechanism.

#### *Flexible Loading*

The loading is assumed to be flexible enough like an embankment so that it exhibits no restrains against the velocity or displacement of the soil mass. The theoretical bearing capacity of the soil mass under a footing was ideally derived by Prandtl and is equal to  $Q_f=(\pi+2) c_u =5.14 c_u$ . Before describing the bearing capacity results for the reinforced cases, the computed bearing capacity of the footing employing rigid plastic finite element method (RPFEM) is discussed. In the previous sections, it was shown that the RPFEM solutions require several cycles of iterations, so the aforesaid analytical solutions for an ideal case can be achieved after much iteration. Considering the time and cost constraints, further computation steps are terminated upon achieving fairly accurate results (fairly accurate refers to personal judgments). Thus, the computed factor of safety for unreinforced soil is 5.168 that is little more than Prandtl's analytical solutions

and assumed to be accurate enough for the practical purposes. The distribution of the velocity vectors is shown in Fig. 4.2.

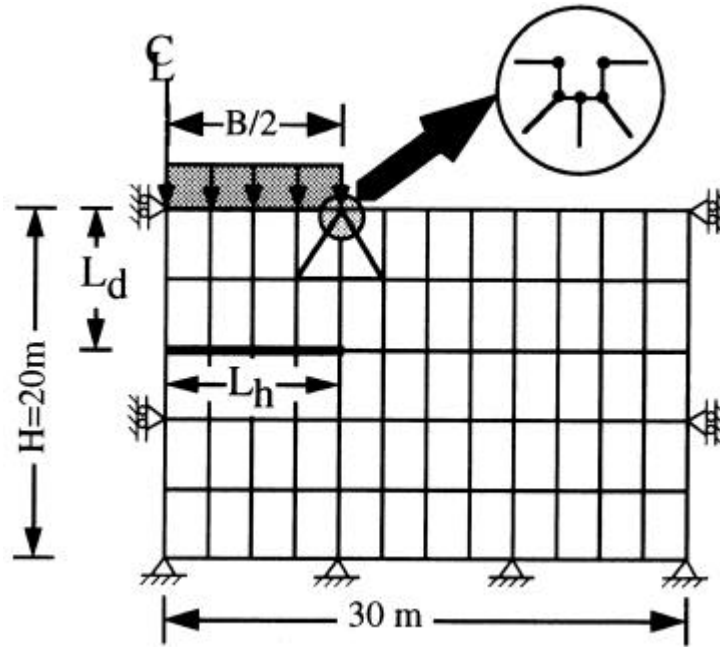


Figure 4.1 Finite element mesh for the bearing capacity problems

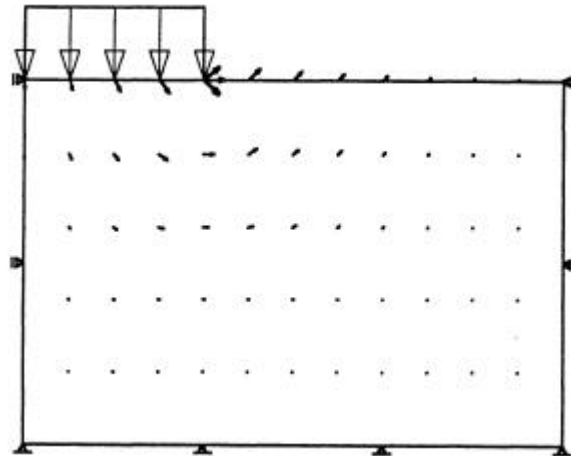


Figure 4.2 Velocity field in an unreinforced soil mass at limit state of soil mass (*flexible footing*)

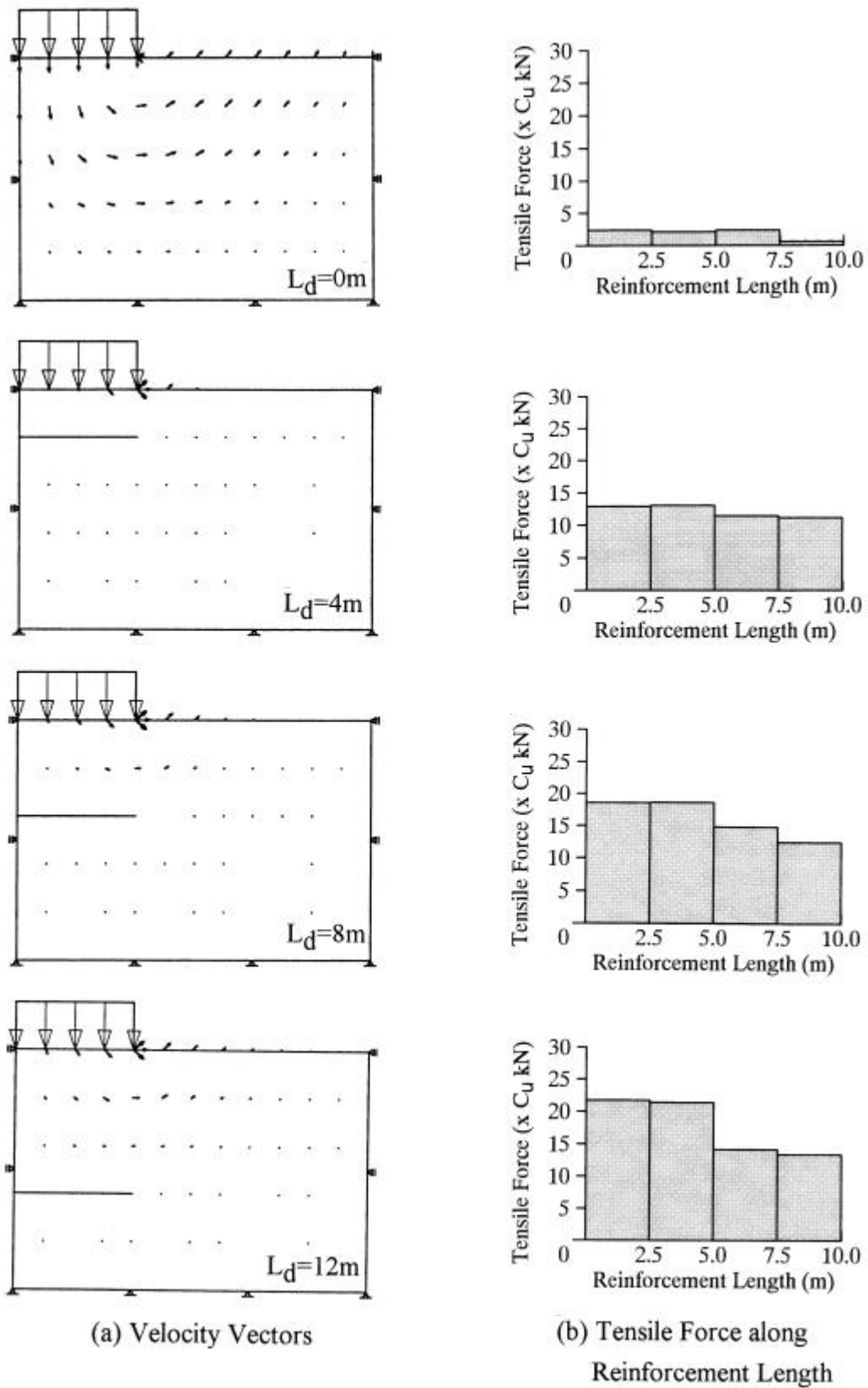


Figure 4.3 Effect of reinforcement on velocity field at limit state of soil mass and axial force distributions along reinforcement (*flexible loading*)

Table 4.1 Computed ultimate bearing capacity and normalized bearing capacity factors for the flexible loading.

Reinforcement Position $L_d$ (m)	Ultimate Bearing Capacity $q_{fc}(x_{c_u})$ (kN/m <sup>2</sup> )	Normalized Bearing Capacity Factor ( $q_{fc}/q_{fu}$ )
-	5.168	1.000
0.0	5.254	1.017
4.0	5.294	1.024
8.0	5.206	1.007

The positions of 20 m long reinforcement (equal to the footing width) are shown in Fig. 4.3. The computed ultimate bearing capacity corresponding to these different positions are tabulated in Table 4.1. The  $c_u$  is undrained shear strength of the clay deposit estimated to  $1/\sqrt{2} \sigma_o$  under plane strain condition. For comparison purposes the computed bearing capacity ( $q_{f\_computed}$ ) is normalized with respect to the bearing capacity of unreinforced ( $q_{f\_unreinforced}$ ) soil media ( $q_{fc}/q_{fu}$ ). Thus, the normalized bearing capacity factor for unreinforced case is unit (i.e. 1.00). In the case of reinforcements placed just under the footing reveals (Table 4.1) an increase in the ultimate bearing capacity compared to the unreinforced case. Further lowering the reinforcement position gradually increases the bearing capacity up to a certain depth and afterwards it starts decreasing that finally reduces to the unreinforced bearing capacity value. The maximum increment after reinforcing the soil is about 2.4% compared to the unreinforced case. Optimum position of the reinforcement was about,  $L_d=4m$  ( $L_d/b=0.4$ ). The very low positioned reinforcement (e.g.  $L_d=12m$ ) has almost no influence over the soil mass because the shearing of soil is confined near the surface. While the higher positions also could not increase the bearing capacity because the directions of the velocity vector around that position before placing the reinforcement was perpendicular to the current reinforcement axis as shown in Fig. 4.3(a). The velocity vectors at and around the optimum position before placing the reinforcement were almost parallel to the current reinforcement axis. This illustrates the best possible orientation for reinforcement is parallel to the velocity vectors. Figure 4.3(b) shows the computed reinforcement force along the reinforcement length for various positions. The axial force gradually increases when the reinforcement positions are lowered.

***Rigid-smooth Footing:***

The footing is assumed perfectly rigid-smooth such that the vertical component of velocities (i.e. along y-direction) just under the footing are equal throughout the plastic flow of soil mass and the velocities are allowed to rotate freely provided the vertical components are maintained equal. Thus, this problem is very similar to the former problem (flexible loading) except the footing rigidity. The other boundary conditions, finite element array and various positions and length of

reinforcement also remained unchanged.

At first, the computation work is carried out for the unreinforced case of the rigid-smooth footing. The ultimate bearing capacity is  $q_f=5.176$  which is almost the same as the flexible loading case ( $q_f=5.167$ ). This  $q_f$  is used in the normalization of the ultimate bearing capacity for comparison with the bearing capacity of reinforced soil cases. The distribution of the nodal velocity vectors in the unreinforced case is shown in the Fig. 4.4.

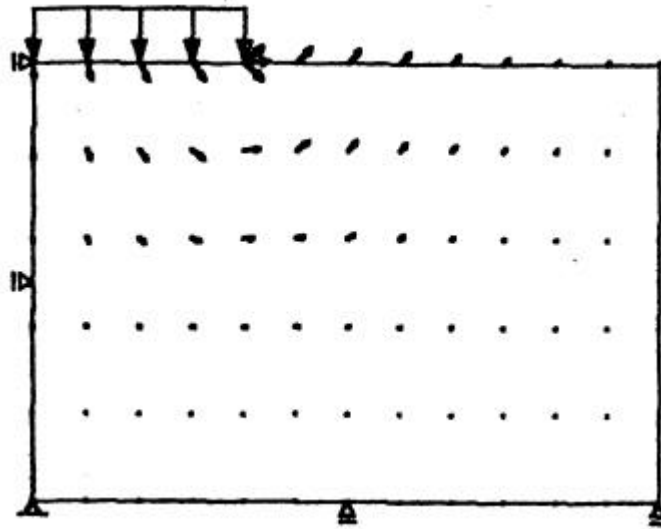


Figure 4.4 Velocity field in an unreinforced soil mass at limit state (*rigid-smooth footing*)

Table 4.2 Computed ultimate bearing capacity and normalized bearing capacity factors for the rigid-smooth footing.

Reinforcement Position $L_d$ (m)	Ultimate Bearing Capacity $q_{fc}(x c_u)$ (kN/m <sup>2</sup> )	Normalized Bearing Capacity Factor ( $q_{fc}/q_{fu}$ )	LEFEM D=0.01m $P_c/P_{uo}$
-	5.172	1.000	1.000
4.0	5.669	1.096	1.372
8.0	5.303	1.025	1.447
12.0	5.187	1.003	1.318
16.0	5.172	1.000	1.145

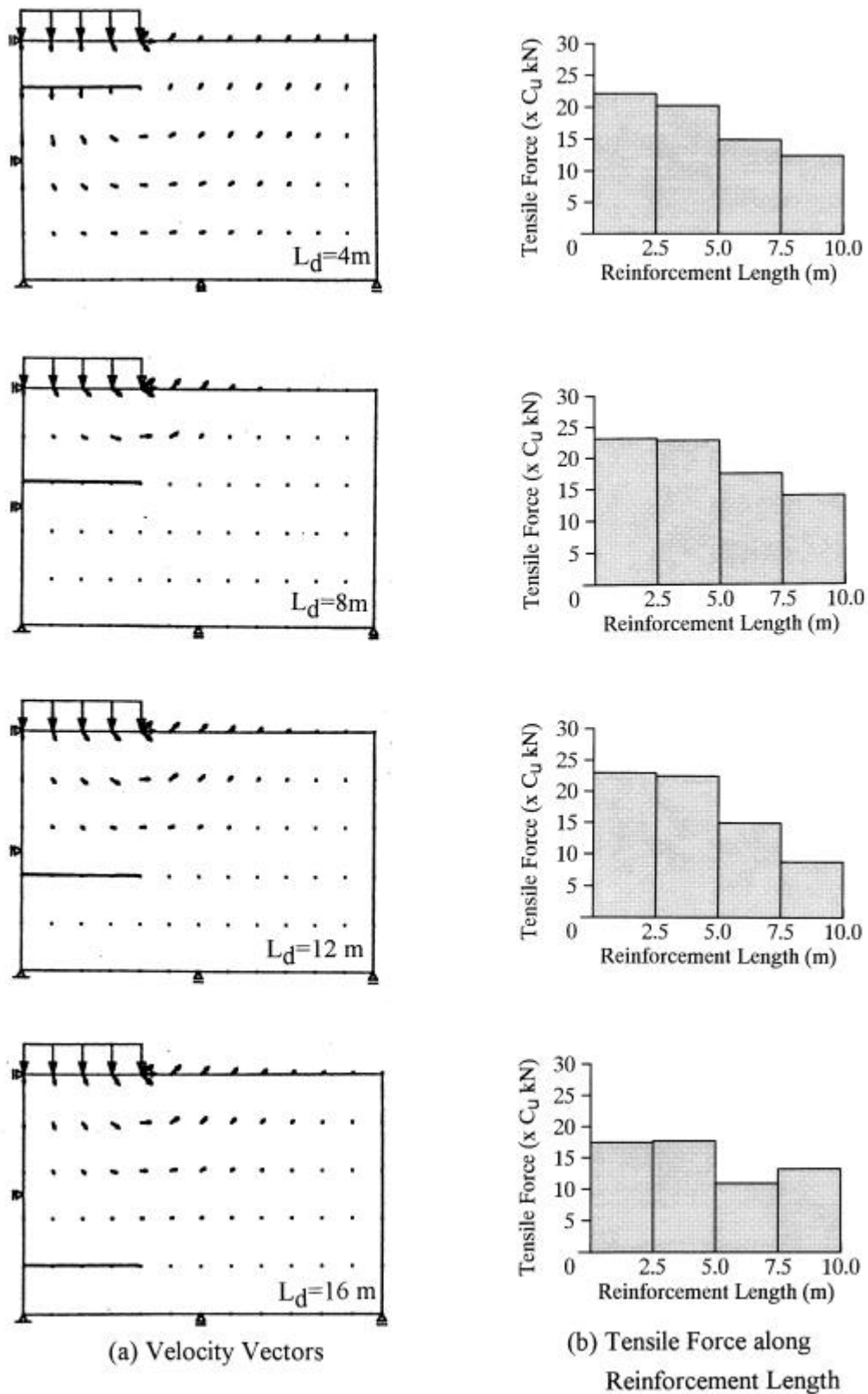


Figure 4.5 Effect of reinforcement on velocity field at limit state of soil mass and axial force distributions along reinforcement (*rigid-smooth footing*)

The positions of 20 m long reinforcement (equal to the footing width) are shown in Fig. 4.5. The computed ultimate bearing capacity corresponding to these different positions are tabulated in Table 4.2. The normalized bearing capacity factors ( $q_{f\_computed} / q_{f\_unreinforced}$ ) are also presented in the same table. The reinforcement placed under the footing ( $L_d=4m$ ) reveals substantial increment (about 10%) in the ultimate bearing capacity compared to the unreinforced case. Further lowering the reinforcement position gradually decreases the ultimate bearing capacity,  $q_f$ , which finally reduces to the unreinforced bearing capacity value. Optimum position of the reinforcement is  $L_d=4m$  ( $L_d/b=0.4$ ) where maximum increment in the bearing capacity is about 10%. The nodal velocity vectors are shown in Fig.4.5 for each cases mentioned in the table. The lowermost reinforcement ( $L_d=16m$ ) shows no influence over the soil mass because of the localized shearing of the soil near the footing. In this case also maximum ultimate bearing capacity,  $q_f$  is obtained for the reinforcement position where the velocity vectors before placing the reinforcement were almost parallel to the current reinforcement axis. This also support the best orientation for a reinforcement noted in the previous example. Figure 4.5 shows the computed axial force along the reinforcement length for various reinforcement positions. The axial force gradually increased when the reinforcement positions are lowered up to the optimum and further lowering resulted gradual decrease in the ultimate bearing capacity,  $q_f$  to the value for the unreinforced case.

### ***Rigid-rough Footing:***

The footing is assumed perfectly rigid such that the vertical component of velocities (i.e. along y-direction) just under the footing is equal at the limit equilibrium state of the soil mass, same as in the previous example. In this case, the lateral component of velocities under the footing are not allowed to rotate which means  $\dot{u}_h = 0$ . This problem is very similar to the previous example (rigid-smooth) except the footing smoothness. The other boundary conditions, finite element array and various positions and length of reinforcement also remained same.

Similar to the previous examples, this example also starts with the computation for the unreinforced soil. The computed ultimate bearing capacity is  $q_f=5.248$  which is higher than the rigid-smooth case ( $q_f=5.171$ ) because of the rough footing. Ultimate bearing capacities computed later in the reinforced cases are normalized with respect to this unreinforced bearing capacity as in earlier examples. The distribution of the nodal velocity vectors in the unreinforced case is shown in the Fig. 4.6.

The reinforcement positions are similar to the previous cases (see Fig.4.5). The computed ultimate bearing capacity and the normalized bearing capacity factors are tabulated in Table 4.3. The reinforcement placed under the footing reveals an increase in the ultimate bearing capacity compared to the unreinforced case. Further lowering the reinforcement position gradually increases the bearing capacity up to certain depth ( $L_d=8m$ ) and afterwards it starts decreasing

which finally reduced to the unreinforced bearing capacity value. The maximum increment after reinforcing the soil is about 13% compared to the unreinforced case. The optimum position of the reinforcement was about,  $L_d=8\text{m}$  ( $L_d/b=0.8$ ). The nodal velocity vectors (Fig.4.7a) are similar to the previous examples. Negligible effect of the lower positioned reinforcement was observed which can be attributed to the localized shearing of soil near the footing toe. Figure 4.7(b) resembles similarity with the axial force distribution patterns illustrated in the previous examples (see Fig. 4.5b). The reinforcement force gradually increases as the reinforcement positions are lowered up to the optimum position. Further lowering of the reinforcement position after the optimum position also gradually reduces the reinforcement forces as shown in Fig.4.7.

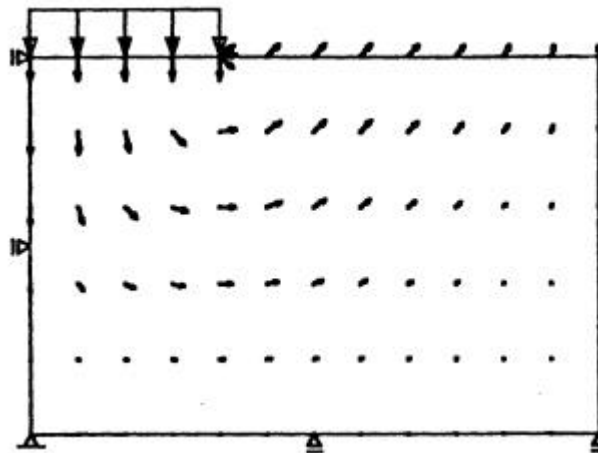


Figure 4.6 Velocity field in an unreinforced soil mass at limit state.  
(rigid-rough footing)

Table 4.3 Computed ultimate bearing capacity and normalized bearing capacity factors for the rigid-rough footing.

Reinforcement Position $L_d$ (m)	Ultimate Bearing Capacity $q_{fc}(x_{c_u})$ (kN/m <sup>2</sup> )	Normalized Bearing Capacity Factor ( $q_{fc}/q_{fu}$ )	LEFEM D=0.01m $P_c/P_{uo}$
-	5.248	1.000	1.000
4.0	5.868	1.114	1.351
8.0	5.956	1.131	1.517
12.0	5.432	1.031	1.392
16.0	5.286	1.003	1.177

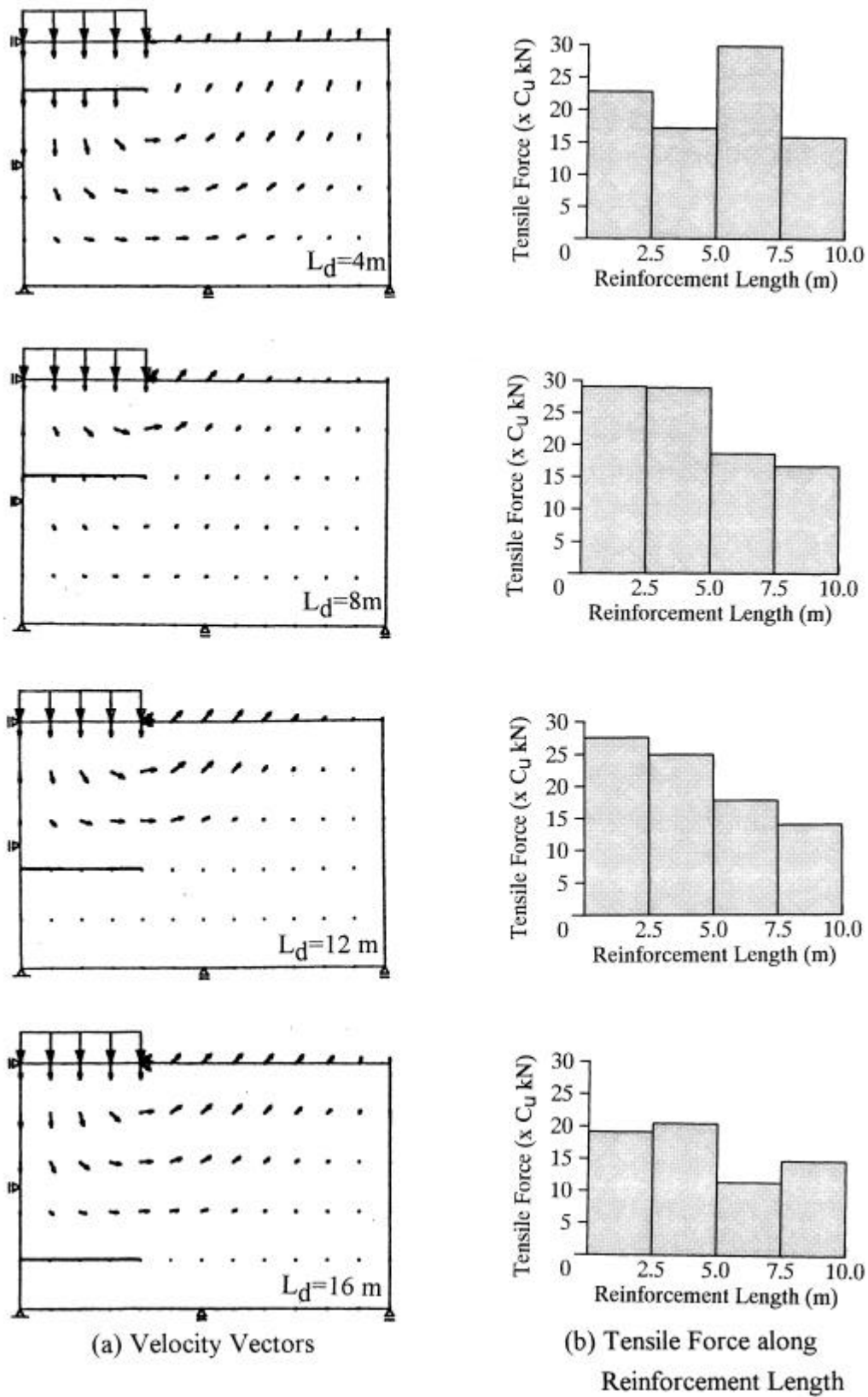


Figure 4.7 Velocity field in reinforced soil mass and axial force distributions at the limit state of the reinforced soil structure (*rigid-rough footing*)

## DEFORMATION ANALYSIS

The deformation analysis in this research deals mainly with the initial load~settlement relations and the displacement field computations. The computations (Figs. 4.8~4.12) are based on the linear elastic finite element method (LEFEM), discussed in the preceding chapter, Chapter III. The reinforcement positions and length remained same as mentioned in the preceding bearing capacity problems. The Young's modulus of elasticity is computed based on an empirical equation,  $E=210 \times C_u = 210 \times 9.8 = 2058 \text{ kPa}$ . The soil is assumed fully saturated, thus, the Poisson's ratio,  $\nu$ , is assumed equal to 0.5 as an incompressible material ( $\epsilon_v=0$ ).

The displacement field of the unreinforced plain soil mass, loaded through rigid footing under smooth and rough surfaces is illustrated in Fig. 4.8. Likewise, the computed displacement field (Figs. 4.9~10) corresponding to reinforced soil cases are shown in Figs. 4.9~10. Similarly, computed footing stress-settlement relations for the unreinforced and the reinforced soil foundations are presented in Figs. 4.11 and 4.12, which clearly show that the optimum position giving maximum effect on the footing stress-settlement relations corresponding to the rigid-rough footing is very similar to the bearing capacity problems, while the optimum position in the case of the rigid-smooth footing is deeper than the bearing capacity problem.

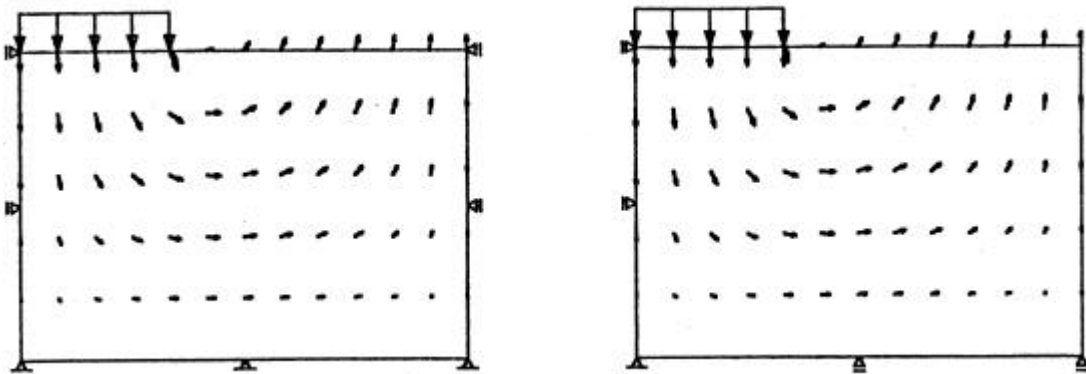
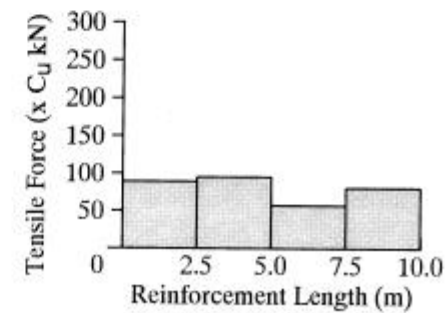
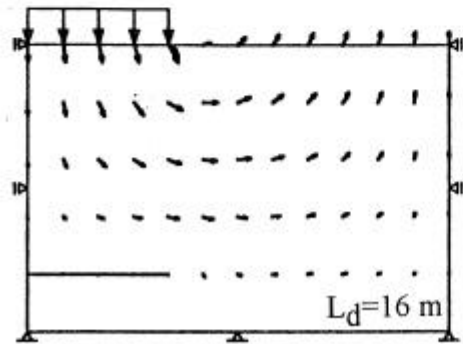
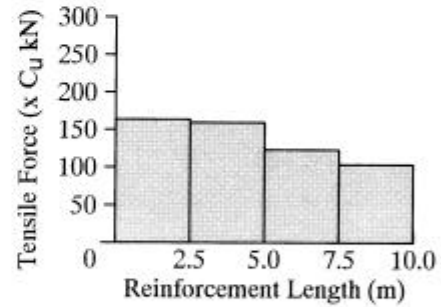
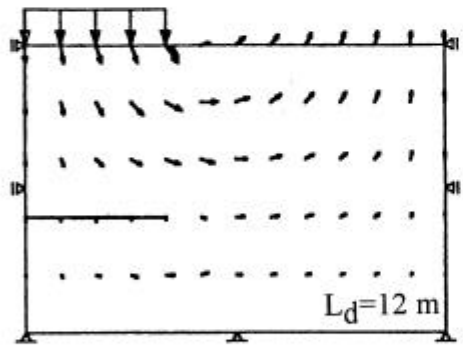
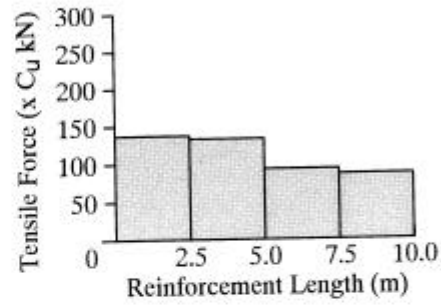
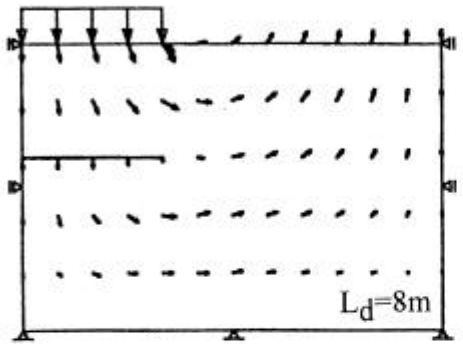
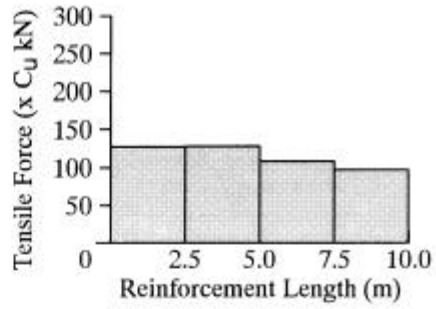
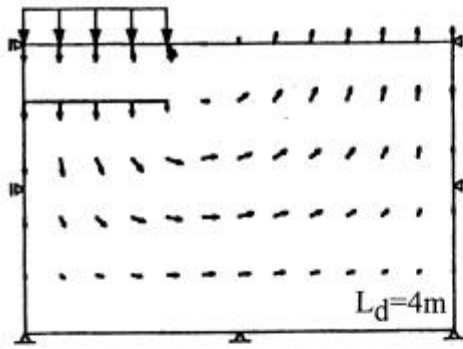


Figure 4.8 Displacement field in unreinforced soil mass based on LEFEM.

Figures 4.9(a) and 4.10(a) clearly show that the influence area is wide for all the reinforcement positions. Compared to the velocity field at the limit state, it may be considered as one major contrast. Two distinct displacement fields could be noticed either side of the reinforcements placed at or around the optimum positions. Such a effect could not be noticed for the reinforcements positioned either very close to the footing or at very low elevations.



(a) Displacement Field

(b) Tensile Force along Reinforcement Length

Figure 4.9 Displacement field in the reinforced soil mass and axial force distributions along reinforcements (*rigid-smooth footing*)

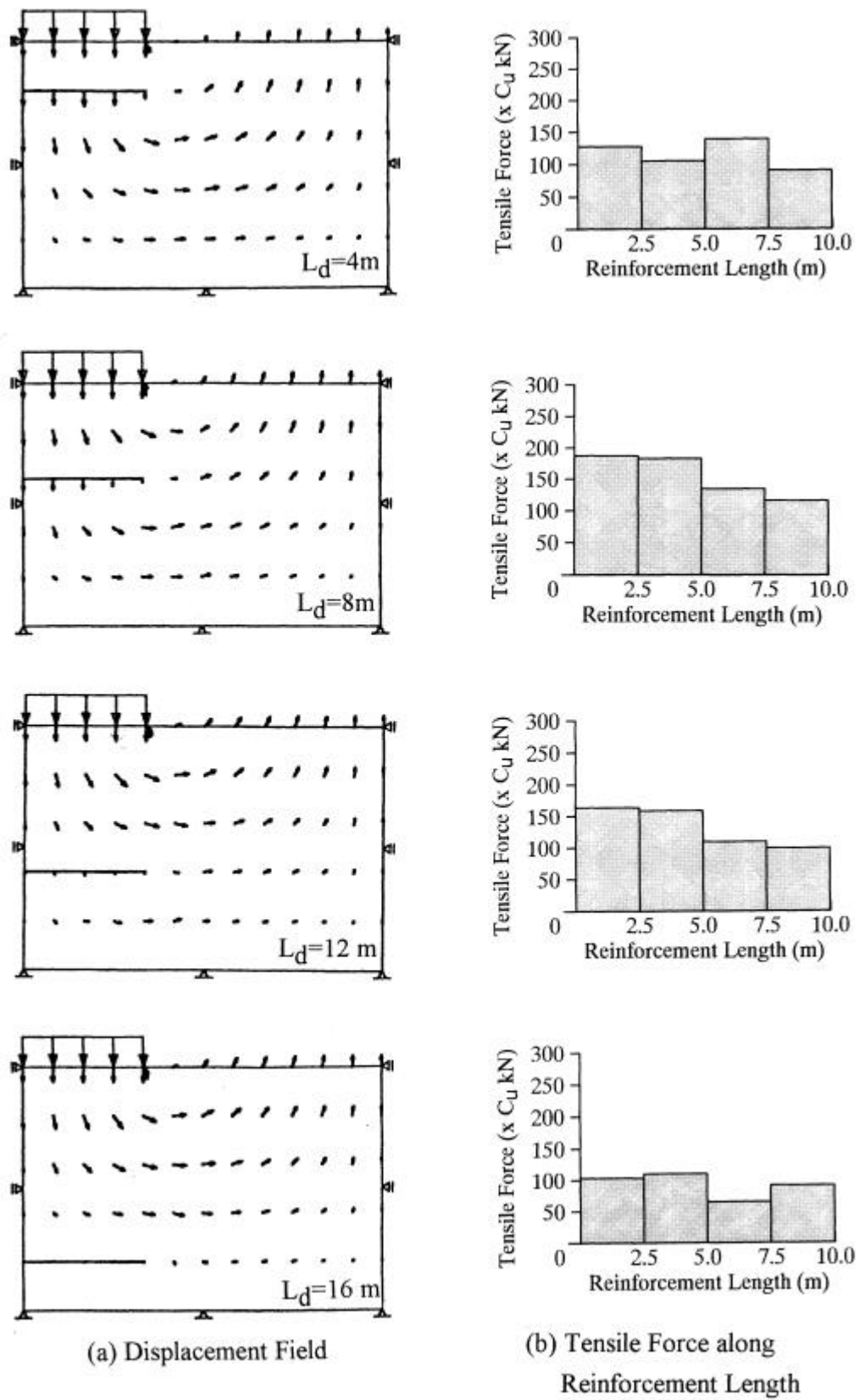


Figure 4.10 Displacement field in the reinforced soil mass and axial force distributions along reinforcements (*rigid-rough footing*)

Corollary, the footing stress is very high for the reinforcement positions where displacement fields are separated into two distinct zones either side of the reinforcements. The magnitudes and distribution pattern of the reinforcement tensile force are almost similar for all the reinforcement positions. The tensile force distribution pattern in the reinforcement is very similar to the patterns observed at the limit state, i.e. bearing capacity problems.

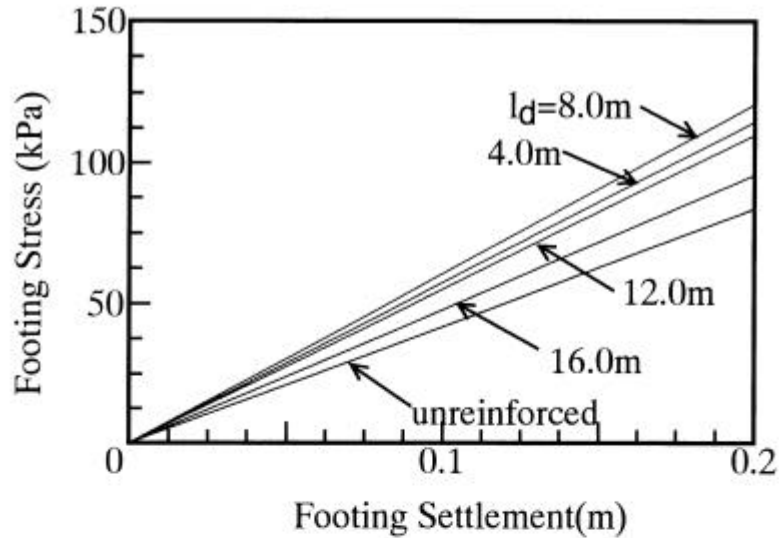


Figure 4.11 Footing stress versus footing settlement relation. (rigid-smooth footing)

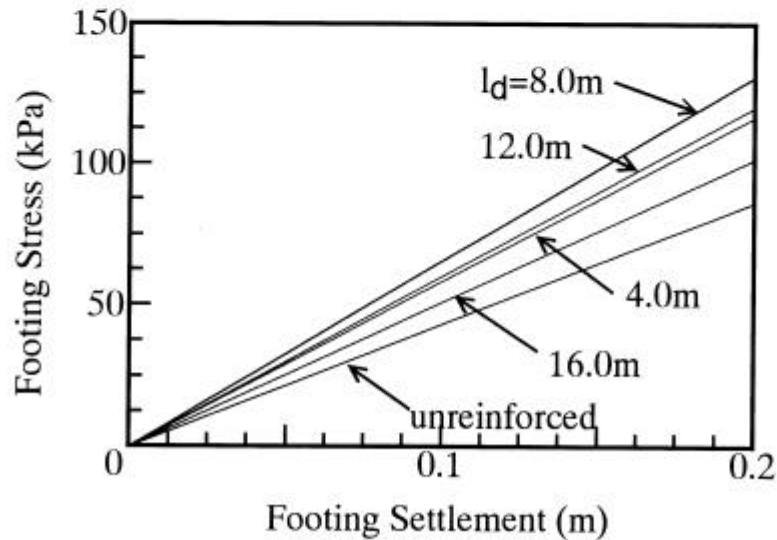


Figure 4.12 Footing stress versus footing settlement relation based on LEFEM. (rigid-rough footing)

### 4.2.3 Clay: *Linearly increasing Shear Strength along Depth*

#### *General*

The normally consolidated clay in nature exhibits linear increase in the undrained shearing strength along the depth. It can be equivalently represented by multi-layered system as shown in Fig.4.13. Asaoka and Kodaka (1993) have illustrated the solution procedure using RPFEM. In this study, the same procedure is employed to solve the reinforced soil when the undrained shear strength of clay increases linearly with depth. For simplicity, the finite element array, the boundary conditions and the loading pattern assumed to be same as in the earlier examples of the homogeneous clay sub-section. The soil strength on the surface is equal to the strength of the homogeneous clay ( $c_u=9.8\text{kPa}$ ). It increases linearly with depth and becomes doubled ( $c_u = 2 \times 9.8 = 19.6\text{kPa}$ ) at the bottom of the soil. The shear strengths assigned to different finite elements at the corresponding elevations assuming the equivalent multi-layered system is shown in Fig.4.13.

In this soil type, only two case: the flexible loading and the rigid-rough footing are presented. The trend of the results obtained employing the proposed methodology is similar to the earlier examples, therefore, only these two cases are illustrated for the sake of completeness.

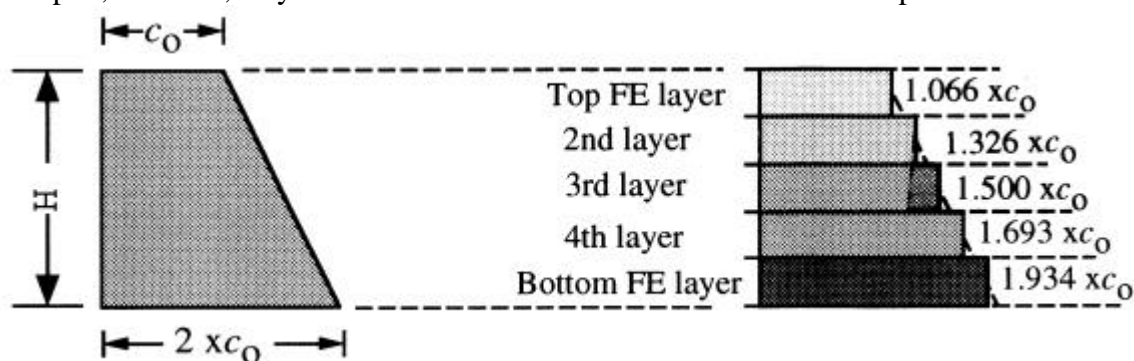


Figure 4.13 Discretization of the linearly increasing shear strength along depth.

#### ***Flexible Loading:***

Flexible loading similar to the first example explained for the homogeneous clay is considered. Before describing the bearing capacity results for the reinforced cases, the computed bearing capacity of the unreinforced soil mass employing the rigid plastic finite element method (RPFEM) is briefed. The computed ultimate bearing capacity for the unreinforced soil is 5.643. The distribution of the velocity vectors is shown in the Fig. 4.14. It clearly shows the influence of increasing shear strength. The failure zone is exclusively localized near the surface especially around the footing edge.

The reinforcement length and positions here, too, are similar to the earlier examples. The

computed ultimate bearing capacity and the normalized bearing capacity factors ( $q_{f\_computed}/q_{f\_unreinforced}$ ) corresponding to these different positions are tabulated in Table 4.4. The result clearly reveals that the lower positioned reinforcements have no influence over the bearing capacity as well as the influence area before and after reinforcing the soil (Fig. 4.15a). Interestingly, the reinforcement force still increases gradually as the reinforcement position is lowered.

Table 4.4 Computed ultimate bearing capacity and normalized bearing capacity factors in the case of the flexible-loading.

Reinforcement Position $L_d$ (m)	Ultimate Bearing Capacity $q_{f_u \times c_u}$ (kN/m <sup>2</sup> )	Normalized Bearing Capacity Factor $(q_{f_u}/q_{f_c})$
-	5.643	1.000
0.0	6.202	1.099
4.0	5.643	1.000
8.0	5.643	1.000
12.0	5.643	1.000

**Rigid-rough Footing:**

The vertical component of the velocities just under the rigid-rough footing is equal at limiting equilibrium state of soil. The lateral component of velocities under the footing are always kept zero,  $\dot{u}_h = 0$ . This problem is very similar to the last example (rigid-rough footing) described under the homogeneous clay problems. The difference is due to the linearly increasing undrained shear strength of the soil in the present example. The other boundary conditions, the finite element array and the various positions and length of the reinforcements also remained same.

Similar to the previous examples, an unreinforced case of rigid-rough footing is investigated first. The reason for higher ultimate bearing capacity,  $q_f=6.871$ , compared to the homogeneous clay under similar rigid-rough footing ( $q_f=5.248$ ) may be attributed to the increasing strength of the soil with depth. The distribution of the nodal velocity vectors is shown in the Fig. 4.16. Which clearly shows the reduced influence area.

The reinforcement positions are shown in Fig. 4.17(a). The computed ultimate bearing capacity and normalized bearing capacity factors corresponding to different positions are tabulated in Table 4.5. The reinforcement placed under the footing reveals an initial increase in the ultimate bearing capacity up to the optimum position and gradually decreases for reinforcements positioned at lower elevations. The pattern of ultimate bearing capacity variation with the

reinforcement position (depth) is very similar to the previous examples. Because of the increasing shear strength of the soil along the depth, the optimum position shifted upward close to the footing (e.g. current  $L_d=4\text{m}$  compared to previous example of the rigid-rough footing in homogeneous example,  $L_{d0}=8\text{m}$ ) The maximum increment after reinforcing the soil is about 25% compared to the unreinforced case, while in the homogeneous clay it was only 13%. The nodal velocity vectors are shown in Fig.4.17 (a) for each cases mentioned in the table. The direction of the velocity vectors at optimum position before and after reinforcing the soil is also similar to the results presented in the homogeneous clay. Fig. 4.17(b) shows the computed reinforcement force along the reinforcement length for various reinforcement positions. The reinforcement force gradually increases when the reinforcement positions are lowered up to the optimum position. Further lowering of the reinforcement position after the optimum position also gradually reduces the reinforcement forces as shown in Fig.4.17 (b).

Table 4.5 Computed ultimate bearing capacity and normalized bearing capacity factors in the case of the rigid-rough footing.

Reinforcement Position $L_d$ (m)	Ultimate Bearing Capacity $q_{fu \times c u}$ (kN/m <sup>2</sup> )	Normalized Bearing Capacity Factor $(q_{fu}/q_{fc})$
-	6.871	1.000
0.0	6.871	1.000
4.0	8.725	1.269
8.0	7.116	1.036
12.0	6.871	1.000

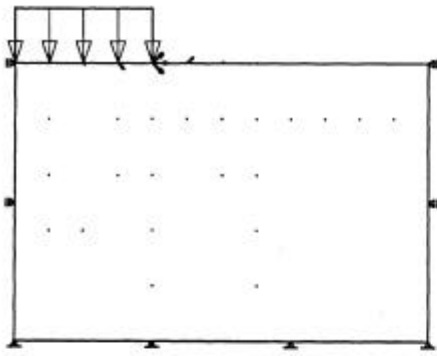


Figure 4.14 Velocity field in a unreinforced soil mass at limit state.  
(flexible loading)

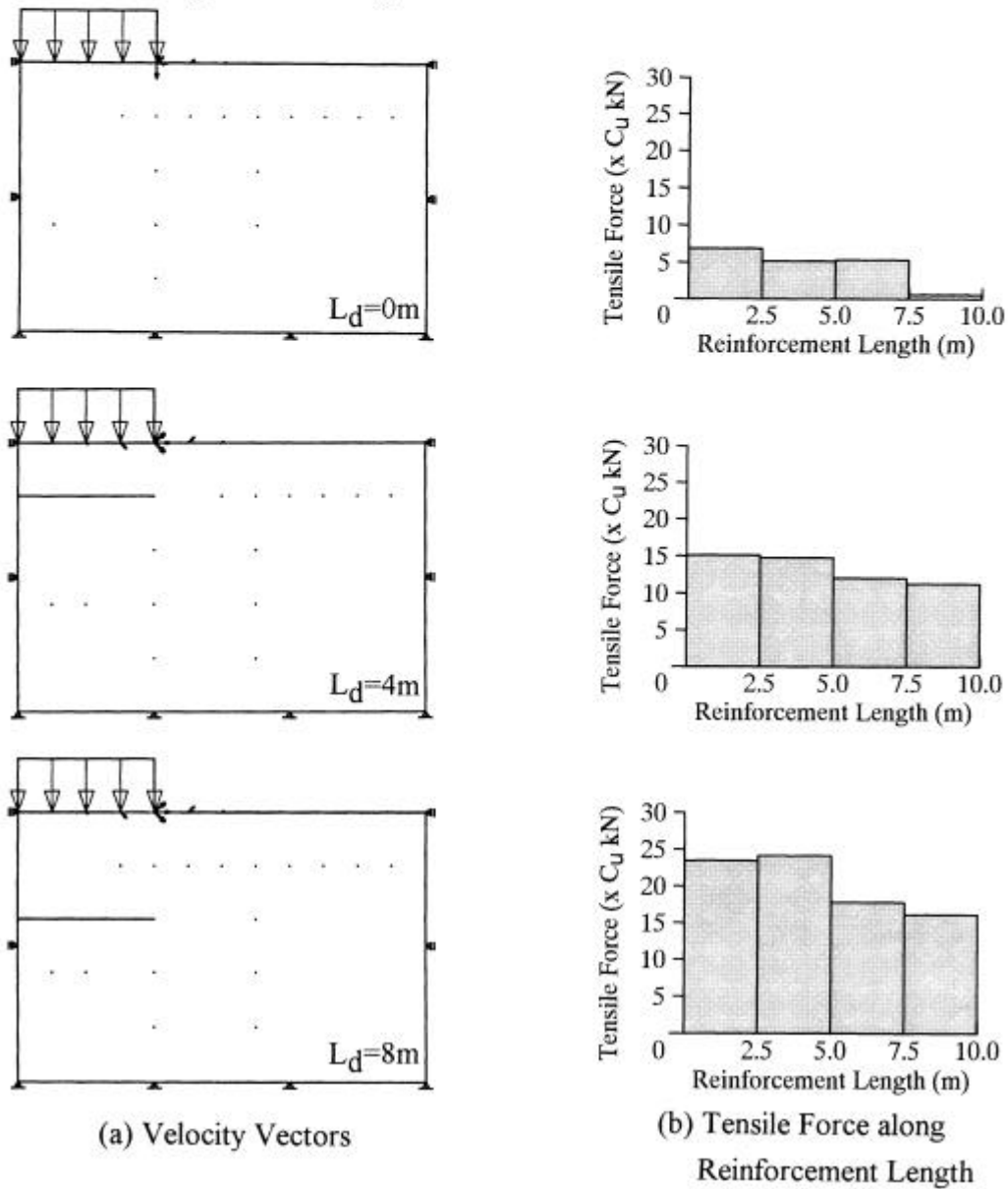


Figure 4.15 Velocity field in reinforced soil mass and axial force distributions at the limit state of the reinforced soil structure (flexible loading)

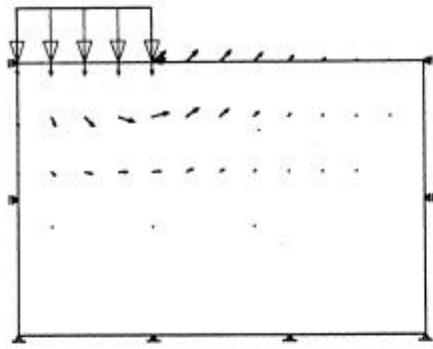
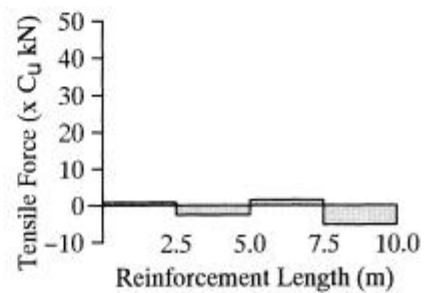
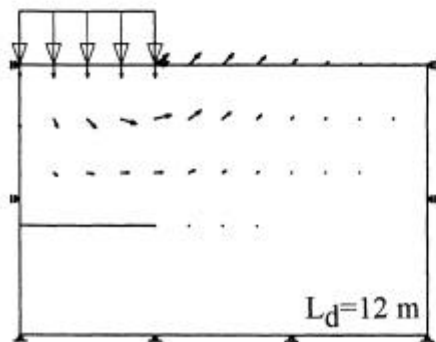
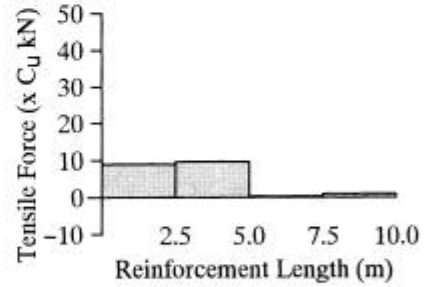
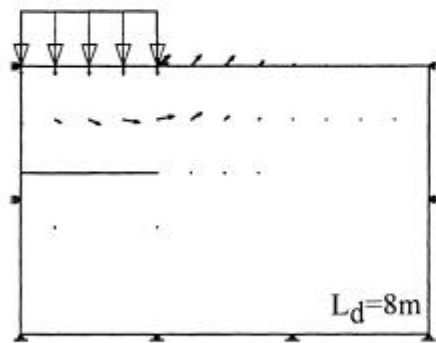
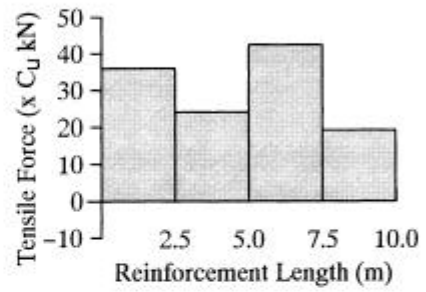
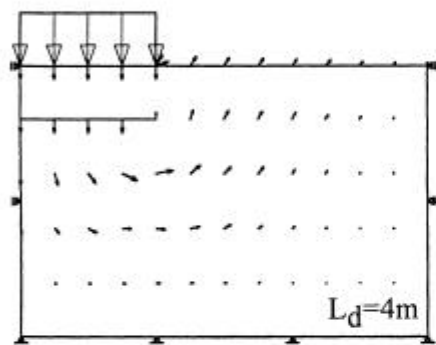


Figure 4.16 Velocity field in an unreinforced soil mass at limit state. (rigid-rough footing)



(a) Velocity Vectors

(b) Tensile Force along Reinforcement Length

Figure 4.17 Velocity field in reinforced soil mass and axial force distributions at the limit state of the reinforced soil structure (rigid-rough footing)

## 4.3 SLOPE STABILITY PROBLEMS

---

### 4.3.1 General

The second representative problem chosen is a slope stability problem. The slope is reinforced by inserting a reinforcing material (e.g. steel bar) from the face like soil nails. For simplicity, first purely cohesive clay under undrained condition (Mises material) is considered, and latter the  $c-\phi$  material, i.e. sandy soil, will be discussed. Velocity boundary conditions are either roller or fixed support types. The failure is caused by the stresses developed due to the body force of soil mass. The isoparametric quadrilateral elements are used in all the examples.

Effect of reinforcement length is investigated by inserting reinforcing member(s) at different elevations. The effect of single reinforcement is also compared with the multiple reinforcements placed simultaneously at different elevations. Safety factor is computed using RPFEM incorporating the proposed mechanism. The factor of safety,  $F_s$  corresponding to the present slope stability problems is the same as load factor,  $\mu$ , introduced in Eq.(3.101). The computed principal stress distributions mean confining stress contours in soil mass and tensile force distributions along the reinforcement are illustrated. The computed nodal velocity vectors are also explained for each case. Detailed explanation is presented in the following sub-sections for each cases dealt with.

### 4.3.2 Purely Cohesive Clay (*Mises Material*)

#### **Example 1: *Horizontal Reinforcement***

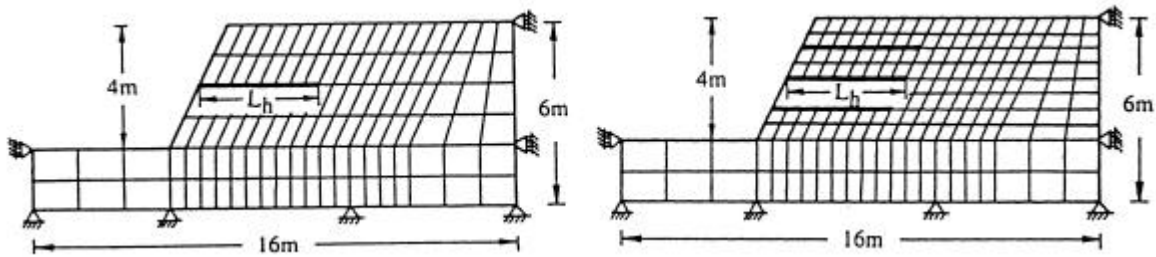
Fig. 4.18 shows a typical finite element array and detailed boundary conditions used in this example. The slope stability problem is considered under plane strain condition assuming close spacing of reinforcements. The grading of the slope face is  $\mathbf{1(Horizontal)} : \mathbf{2(Vertical)}$ , i.e.  $67^\circ$  with horizontal. The soil properties of the Mises material are chosen in such a way that the unreinforced soil under prescribed boundary conditions gives the factor of safety,  $F_s=1.0$ . Thus, the soil properties for the present example are  $c_u=12.3$  kPa and  $\gamma_t=16.3$  kN/m<sup>3</sup>.

Reinforcements are placed horizontally at three elevations as shown in Fig. 4.18(b). In case of single reinforcement, the middle position is only explained. The computed factor of safety corresponding to different length of the reinforcements is plotted in Fig.4.19. The initial rate of increase of the safety factor is slow for relatively shorter reinforcements. The safety factor gradually increases as the reinforcement length is extended and after some length the rate is very rapid (Fig. 4.19). The computed safety factor is also higher when the number of reinforcement is increased to three. It should be noted here that the absolute increase in safety factor is still relatively small compared to  $c-\phi$  material cases discussed later

The computed nodal velocity vectors are also plotted in Fig. 4.21(a); the figure shows that the

influence area widens as the length increases. The tensile force diagram along reinforcement (Fig. 4.21b) also reveals an increase in tensile force magnitudes with respect to the reinforcement length increments. The computed tensile force distribution pattern is very similar to the experimental observations (Nagao et al., 1988 and Hada et al., 1988).

Figure 4.22(a) shows the velocity field and the tensile force distribution along three 5m long reinforcements placed at three different elevations. In this case, computation is carried out with fine FE mesh to avoid the influence of the FE mesh. The FE layers between the consecutive reinforcements are divided into two layers as shown in Fig.4.18 (b). It shows that a clear tensile force distribution can be obtained without any computational disorder thus avoiding the direct interference effect of the reinforcements. The higher confining pressure at lower elevations because of the gravity loading produced higher magnitude in the tensile force distributions for reinforcements placed at lower elevations.



(a) Single Reinforcement Cases

(b) Multiple Reinforcements Cases

Figure 4.18 Finite element array for the stability analysis of the reinforced soil slopes.

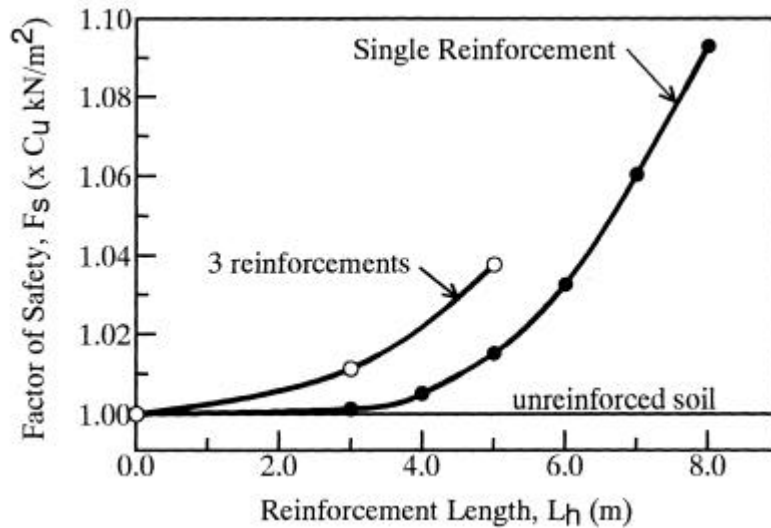


Figure 4.19 Computed factor of safety versus reinforcement length relation in a reinforced purely cohesive clay slope (*Mises material*).

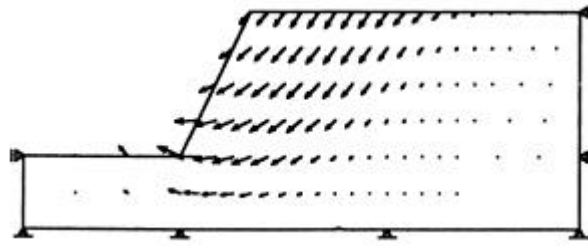


Figure 4.20 Velocity field at limit equilibrium state of the soil mass without any reinforcing material.

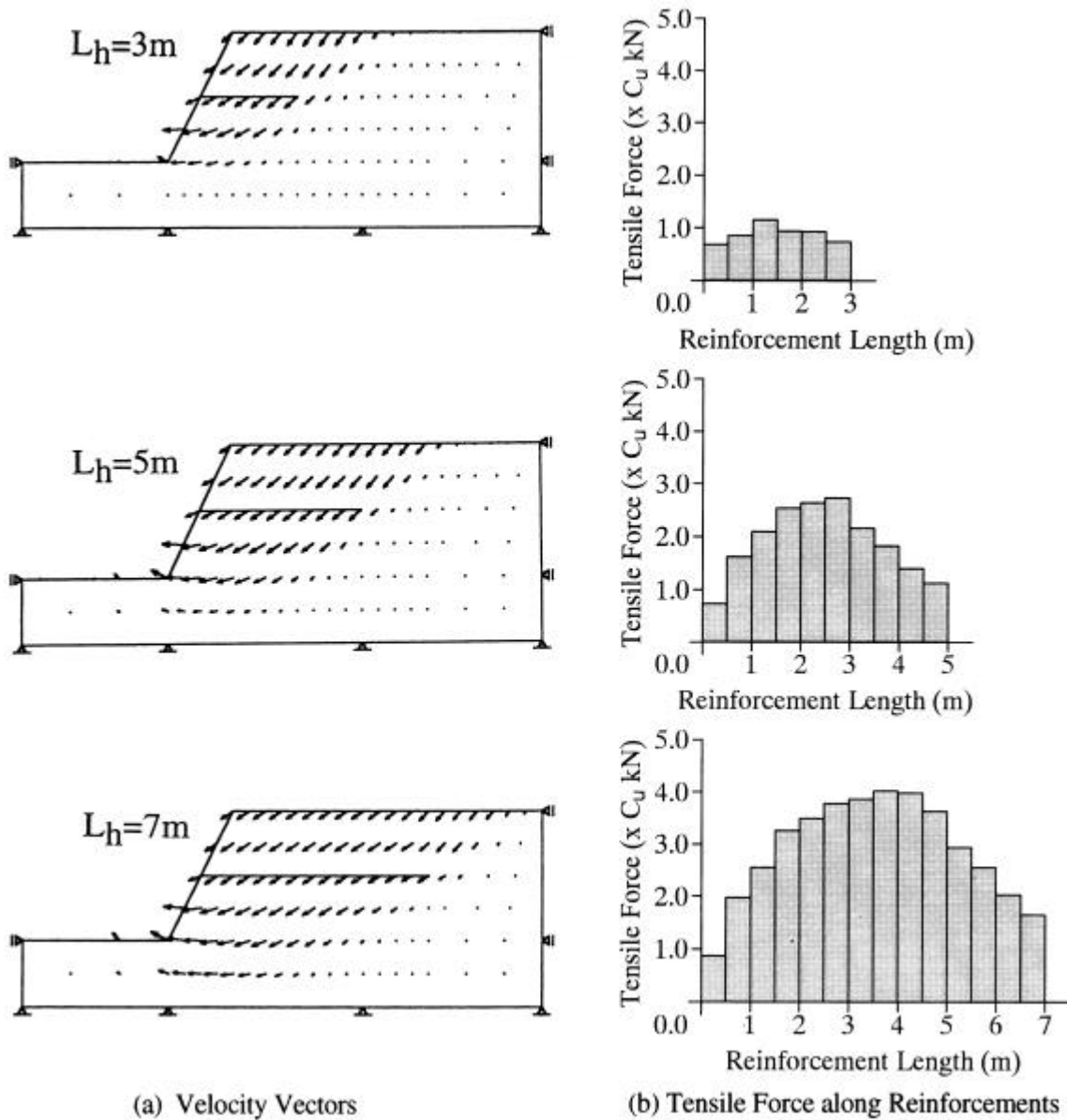
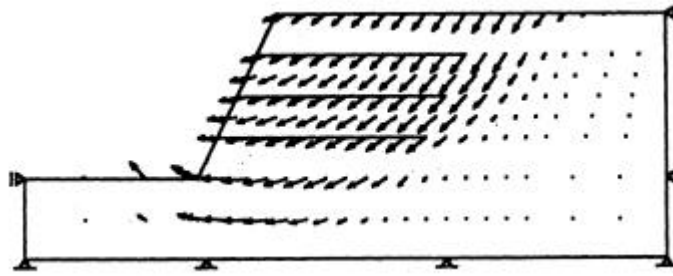
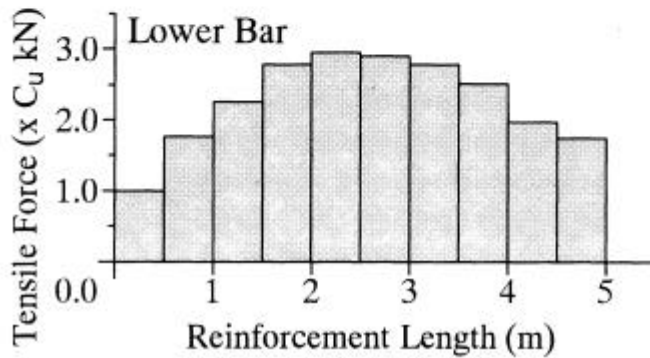
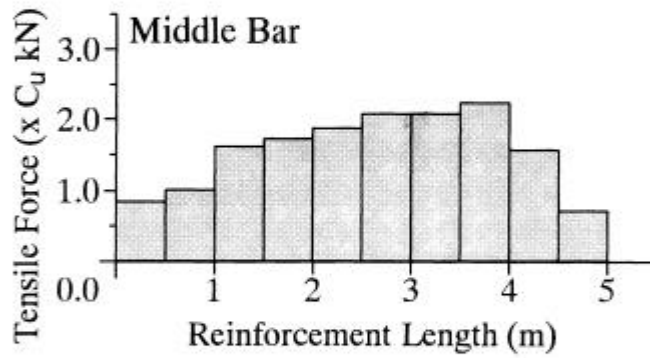
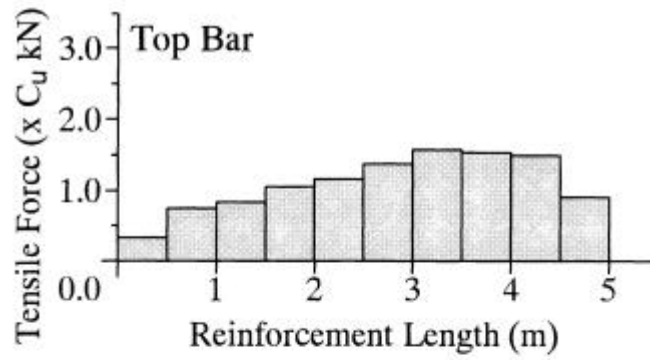


Figure 4.21 Effect of reinforcement lengths on velocity field and the axial force along reinforcements.



(a) Velocity Vectors



(b) Tensile Force along Reinforcements

Figure 4.22 Effect of multiple reinforcements on velocity field and the axial force distribution along the reinforcements.

### **Example 2: *Inclined Reinforcement***

In this example, a reinforcing material is placed at different angles and locations. The length of reinforcement is kept constant, 5m. The total thickness of the soil in previous example is increased by 2m for convenience in placing the reinforcement at different angles. Figure 4.23 shows a typical finite element array and detailed boundary conditions used in this example. The safety factor is computed for three positions (top, middle and bottom) along vertical directions and at five different inclinations corresponding to each position as shown in Fig. 4.24. Factor of safety gradually increases (Fig. 4.24) as the reinforcement position is lowered and or inclination is increased or the number of reinforcements are increased. The figure shows that the lower position is relatively more effective. It should also be noted here that the absolute increase in safety factor is relatively smaller than the frictional ( $c-\phi$ ) material case to be discussed later.

Though the factor of safety for the top, middle and bottom positions are presented; the velocity vectors, the reinforcement force and the principal stress distributions are discussed in detail only for the middle position.

The computed nodal velocity vectors are plotted in Fig. 4.26a; the figure reveals that the failure region goes on widening with respect to increase in the reinforcement inclination. Figures. 4.25b and 4.26b show the principal stresses corresponding to the unreinforced and the reinforced cases respectively. The directions of principal stresses are smoothly changing in unreinforced soil while the principal stress directions in reinforced soil are abruptly rotated around these inclined reinforcements. Such rotation may be attributed to the soil-reinforcement interface friction.

Figure 4.26c shows the tensile force distribution in a reinforcement corresponding to the middle position. The horizontal position gives the parabolic distribution, but, as the inclination of the reinforcement becomes steeper, the tensile force distribution diagram tends to be uniform. Though the maximum tensile force decreases due to the steeper inclinations of the reinforcements, the safety factor is still increasing.

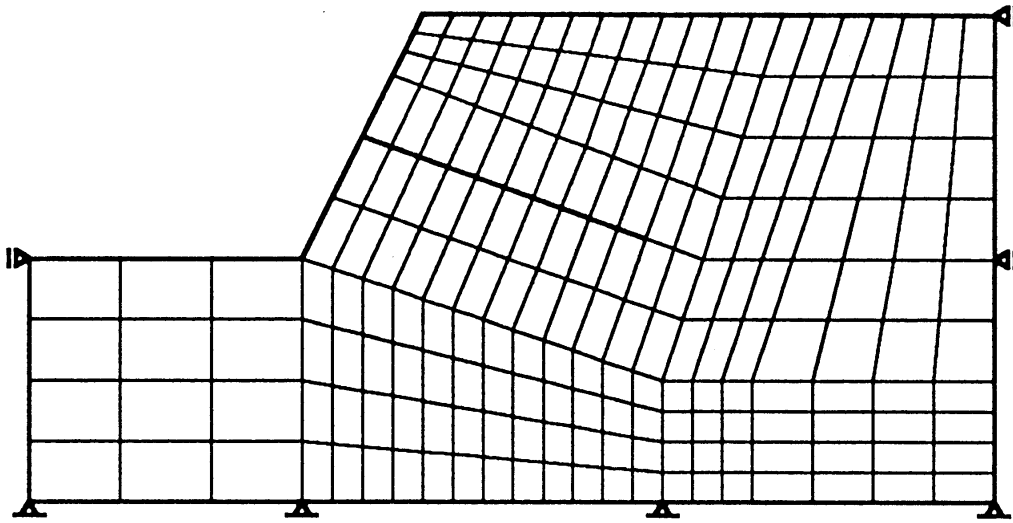


Figure 4.23 A typical finite element array for the slopes reinforced with the inclined reinforcements.

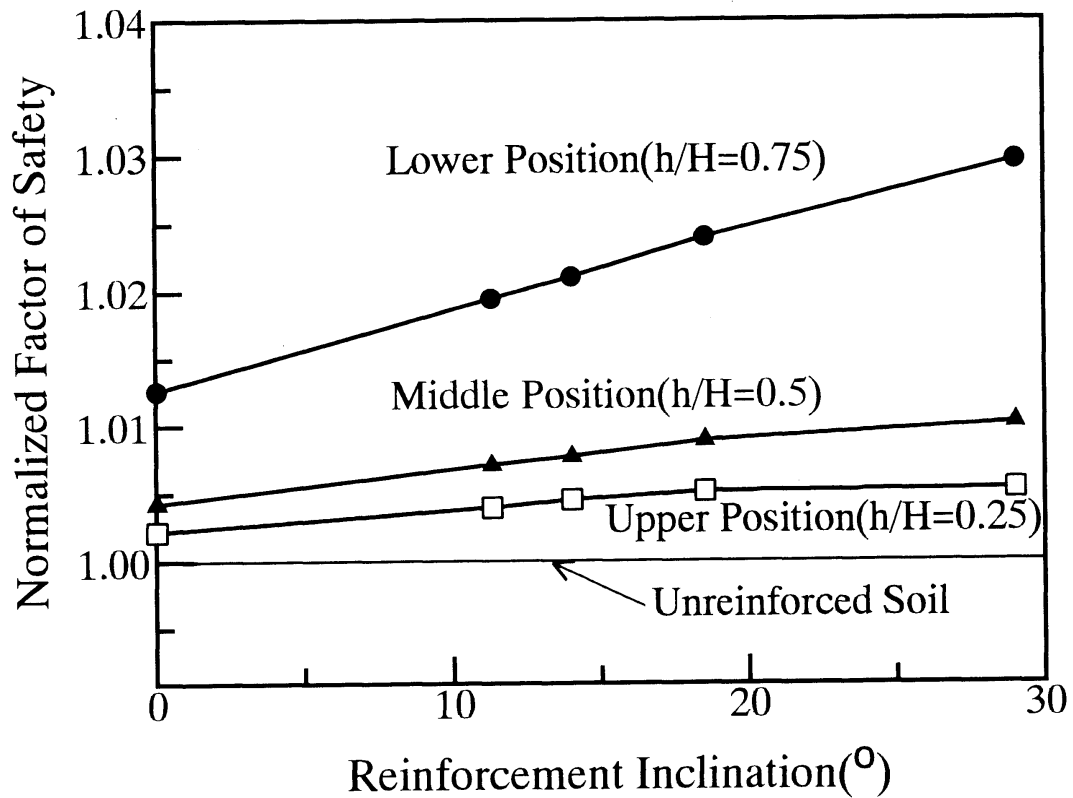


Figure 4.24 Computed factor of safety versus reinforcement inclination relations for a reinforced purely cohesive clay slope (*Mises material*).

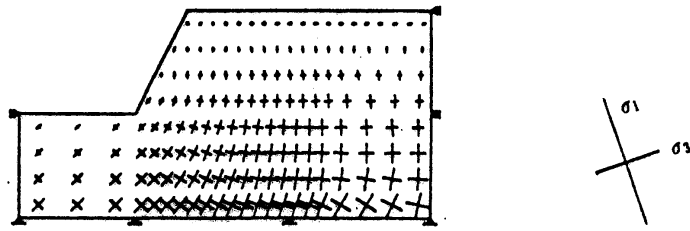
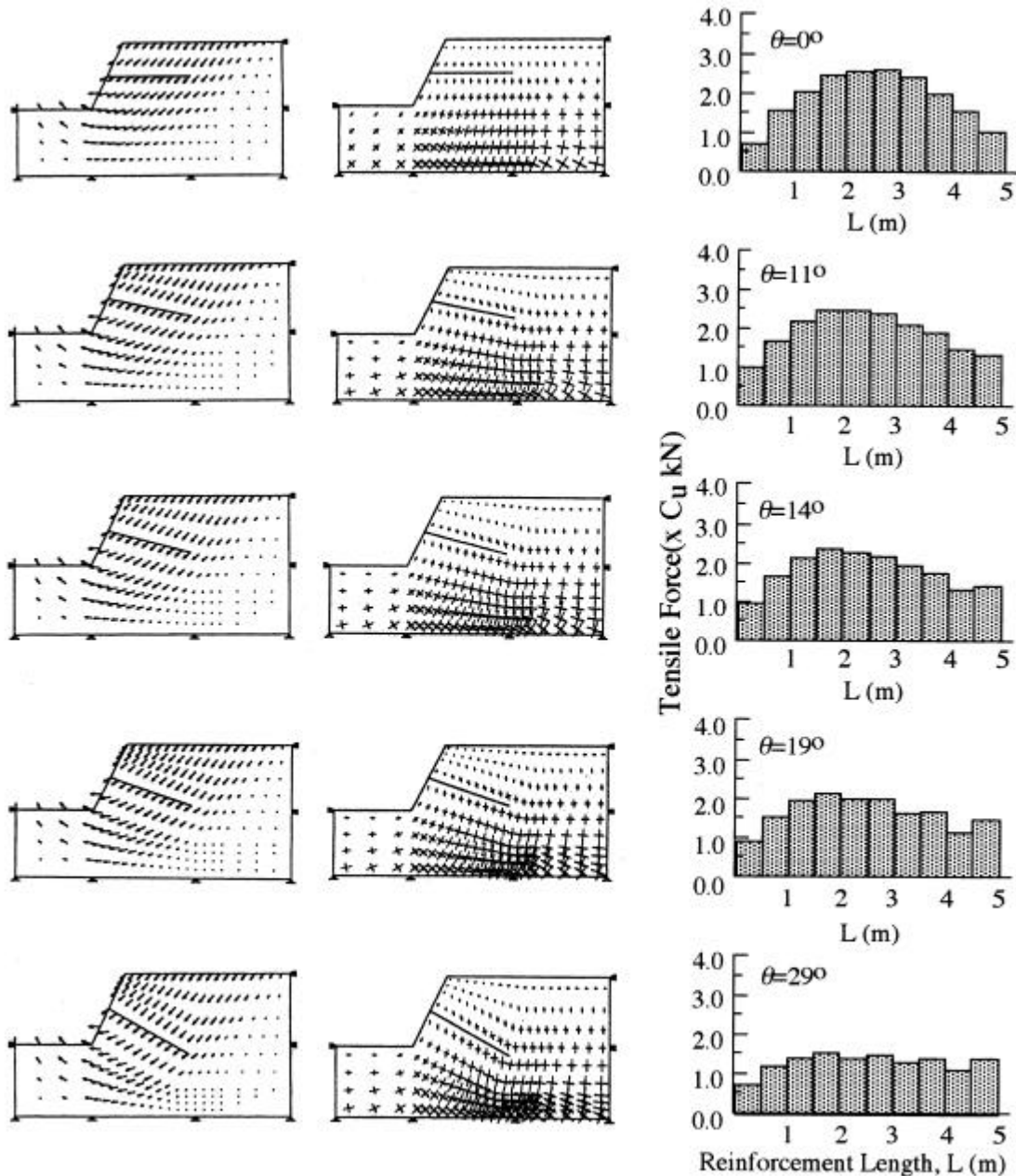


Figure 4.25 Velocity field and principal stress orientations in the unreinforced cohesive clay slope.



(a) Velocity Field      (b) Principal Stresses      (c) Tensile Force along Reinforcements

Figure 4.26 Effect of reinforcement inclinations on velocity field, principal stress orientations and the axial force distribution along reinforcements.

### Example 3: Reinforced Slope with Facing Material

In this example, the facing panels are installed in order to examine the effect of facing on the slope rigidity as shown in Figs. 4.27 & 4.28. Facings are assumed rigid enough; therefore, the formulation for the "no-bending" condition presented in the Chapter III is employed. The facings are discretized in two ways: (a) Panel facing with pin-joints at the connection (Fig. 4.28a). (b) Rigid continuous facing, e.g., full height RCC facing or panel facings with rigid connections at the joints (Fig. 4.28b). The latter type can be modeled by overlapping several basic bending elements in series as shown in Fig.4.28b. As facing is assumed to follow the "no-bending" condition, the distance between nodes representing facing also does not change at the limiting equilibrium state, such that the thickness of the facing does not explicitly appear in the numerical analysis.

The slope configuration is same as in the Example 1 where a 5m long reinforcing material is connected to facing panels (Fig. 4.29). The axial force distributions along reinforcement lengths (Figs. 4.30 & 4.31) and shear force(or bending moment) distributions along facing are computed. The computed bending moment is presented in Fig. 4.32. Very high bending moment at the facing-reinforcement connection clearly reveals the resistance by panel facing to bending due to the lateral earth pressure. The factor of safety in this case is  $F_s=1.036$ . When compared with the no-facing case, the effect of the facing is same as the effect of three reinforcements case without facing (see Tables 4.6 and 4.7).

Table 4.6 Computed safety factor for the facing connected to the single reinforcement cases

Type	Factor of Safety, $F_s$
Unreinforced case	1.000
Reinforcement alone (without facing)	1.015
Reinforcement connected to facing. Facing discretized by technique, T-1	1.025
Reinforcement connected to facing. Facing discretized by technique, T-2	1.039

Effect of the facing connected to multiple reinforcements is investigated, where the facing is discretized by the aforesaid techniques. The velocity vectors and the reinforcement force distributions corresponding to these two techniques are compared with the multiple reinforcements without facing (see Figs. 4.33 & 4.34). The nodal velocity vectors acting on the facing nodes are parallel to each other for the continuous rigid type of facing in contrast to the no-facing case or three reinforcements with facing modeled by the first method. The facing does not exhibit significant effect on the velocity field. The magnitude of the velocity vectors away from toe is very high compared to the no-facing case and the facing discretized by the first technique.

Thus, the soil rotation is above the toe in no-facing case or in pin-jointed panel facing case and the rotation is about the toe when facing is a rigid continuous type. The axial force distribution pattern is parabolic. The lower reinforcement exhibits maximum axial force close to the slope face and gradually decreasing towards the inner end of the reinforcements. The top and middle positioned reinforcements have axial force distribution very similar to the no-facing case. The bending moment diagram (Figs. 4.34 & 4.35) using both the facing discretization technique produces almost similar peaks while the distribution is better represented in the second method.

Table 4.7 Computed safety factor for the facing connected to the three reinforcements

Type	Factor of Safety, $F_s$
Unreinforced case	1.000
Reinforcement alone (without facing)	1.037
Reinforcement connected to facing. Facing discretized by technique, T-1	1.050
Reinforcement connected to facing. Facing discretized by technique, T-2	1.054

In addition to the aforementioned facing discretization techniques, another alternative approach (Fig. 4.36) is also attempted. In this method, the lengths between all nodes on both sides of this panel facing area (Fig.4.36) are assumed to follow only the 'no-length change' condition. The thickness of the facing appears in the numerical analysis (Figs. 4.36 & 4.37). Therefore, both the compressive and the tensile force distributions could be computed. The computed results shown in Fig. 4.38 clearly demonstrate that the inner side of the facing is under tension while outside is under compression. This verifies that the panel facing resists the bending moment induced due to the lateral earth pressure. The factor of safety in this case is  $F_s=1.039$ . As compared with the no-facing case (Fig.4.22), the effect of the facing is same as the effect of the three-reinforcement case without facing.

The velocity vectors and the tensile force distribution along reinforcement shown in Fig. 4.39(b) exhibits similarity with Fig.4.30 (a). The directions of the velocity vectors on the panel facing nodes are restrained due to the existence of facing while the velocity vectors away from the slope toe have relatively wider influence area and larger relative magnitudes. The tensile force distribution near the facing becomes larger than the no-facing case and has almost similar pattern as that observed in many experiments (e.g. Schlosser, 1990 and Tatsuoka et al., 1992).

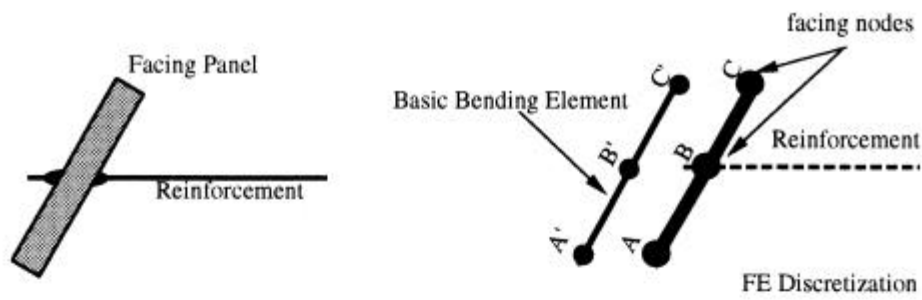
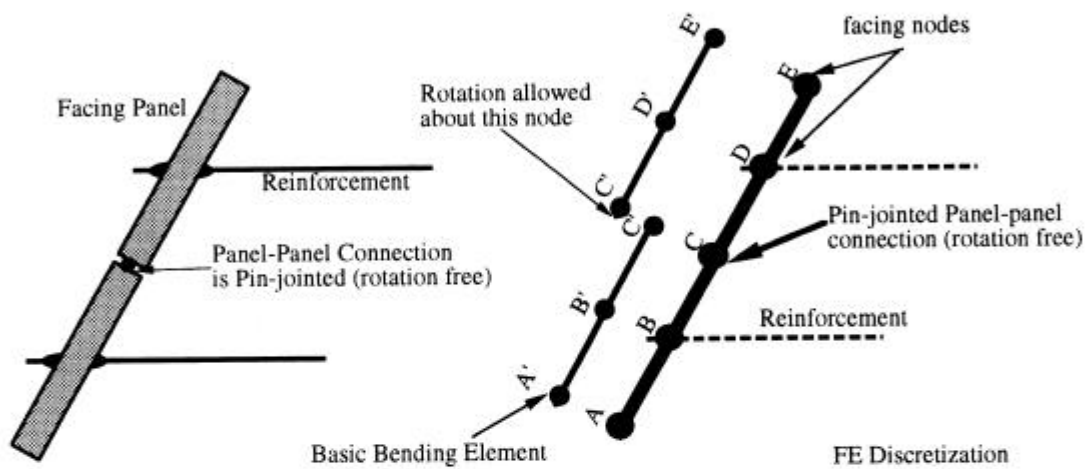
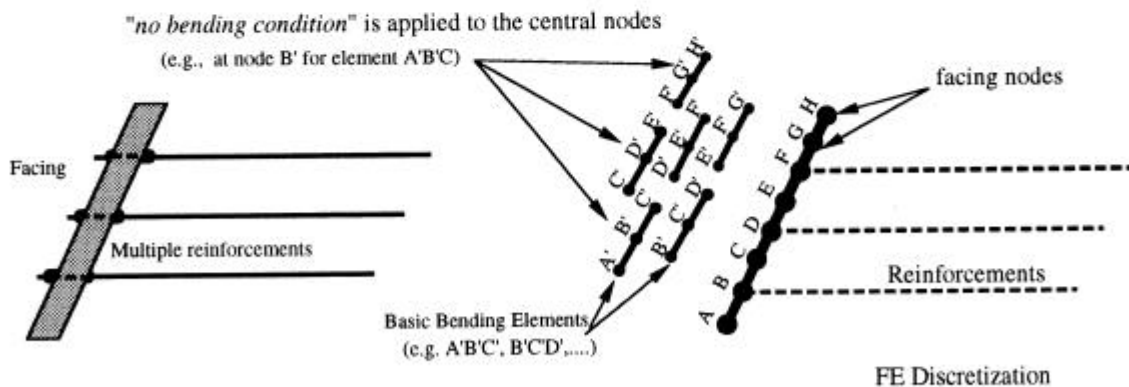


Figure 4.27 FE discretization of a single facing panel as a basic bending element.



Multiple panels having pin joint connection at the panel-panel interface..

(a) Facing Discretization Technique-1



Multiple reinforcements connected to a full height rigid concrete facing or multiple facing panels with rigid panel-panel joints.

(b) Facing Discretization Technique-2

Figure 4.28 FE discretization techniques for a continuous and a discrete rigid facing material.

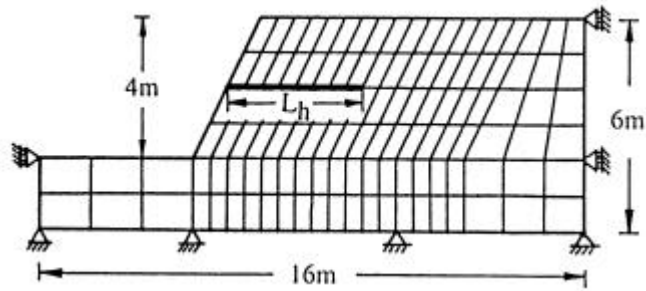


Figure 4.29 A typical finite element array for the reinforced slopes with facing material.

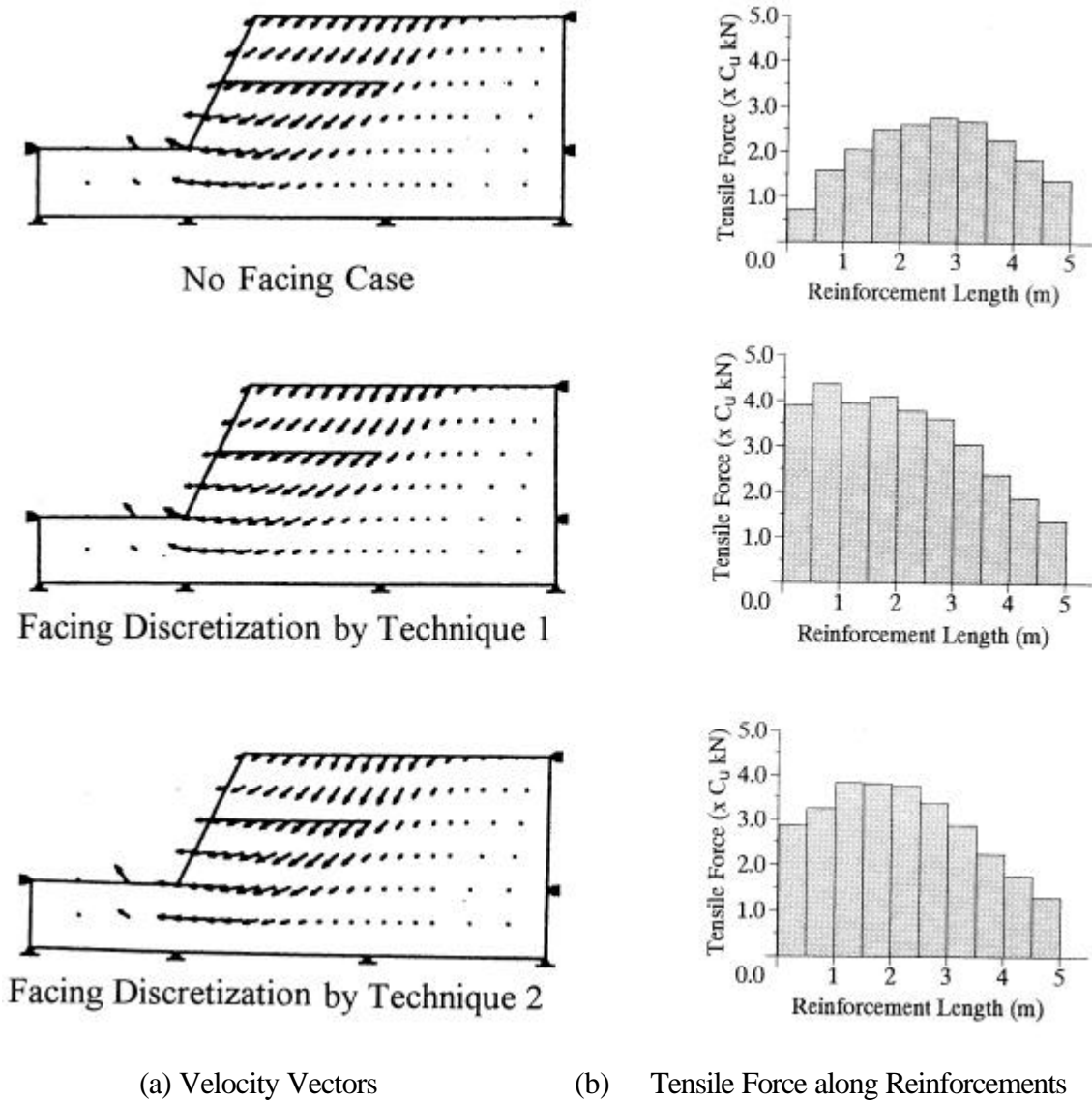


Figure 4.30 Effect of facings on velocity field and axial force distributions in bars.

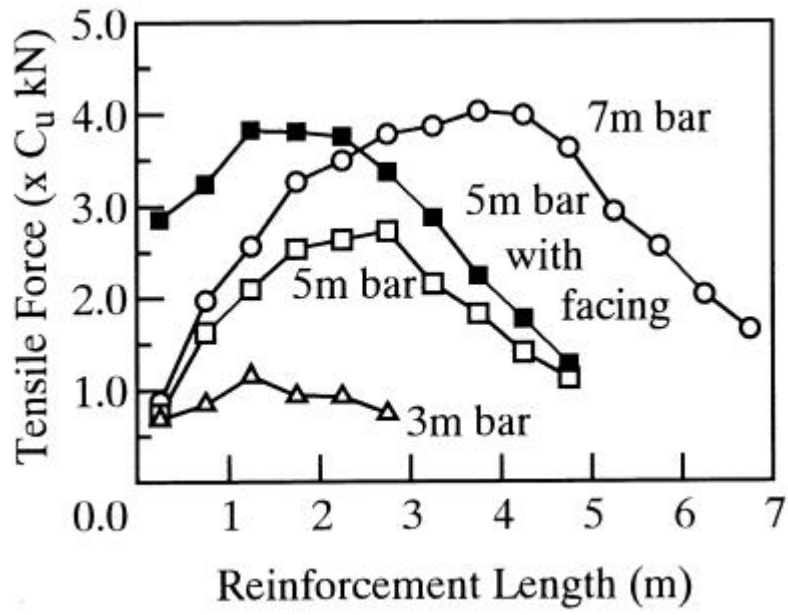


Figure 4.31 Comparisons of axial force distributions along reinforcements with and without facing materials.

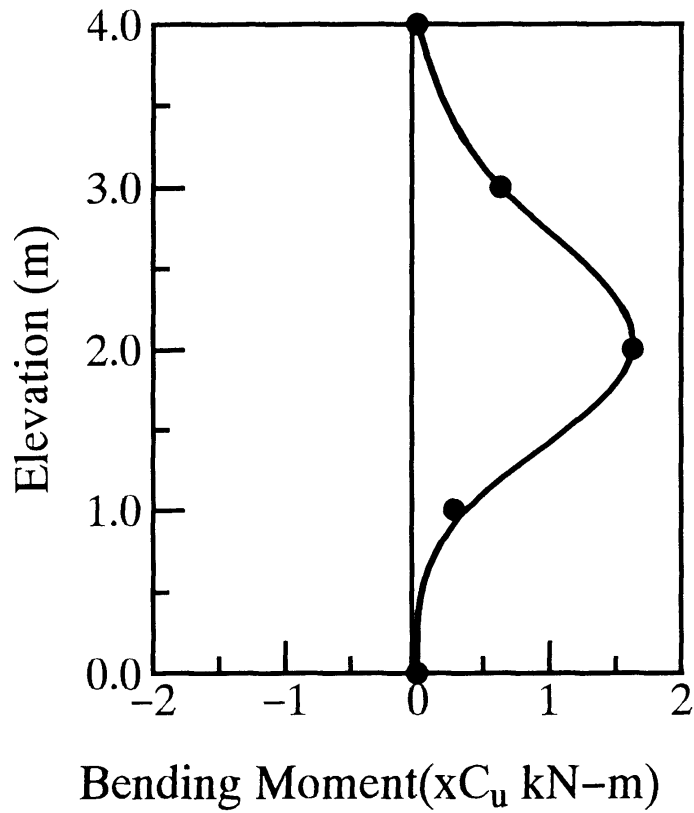


Figure 4.32 Computed bending moment distribution along a facing panel connected to single reinforcement.

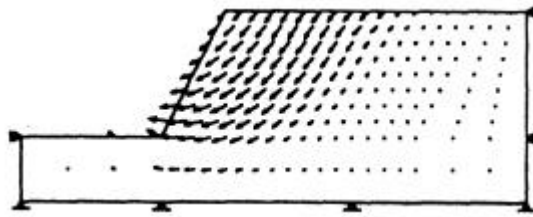


Figure 4.33 Velocity field in the unreinforced soil mass at limit state.

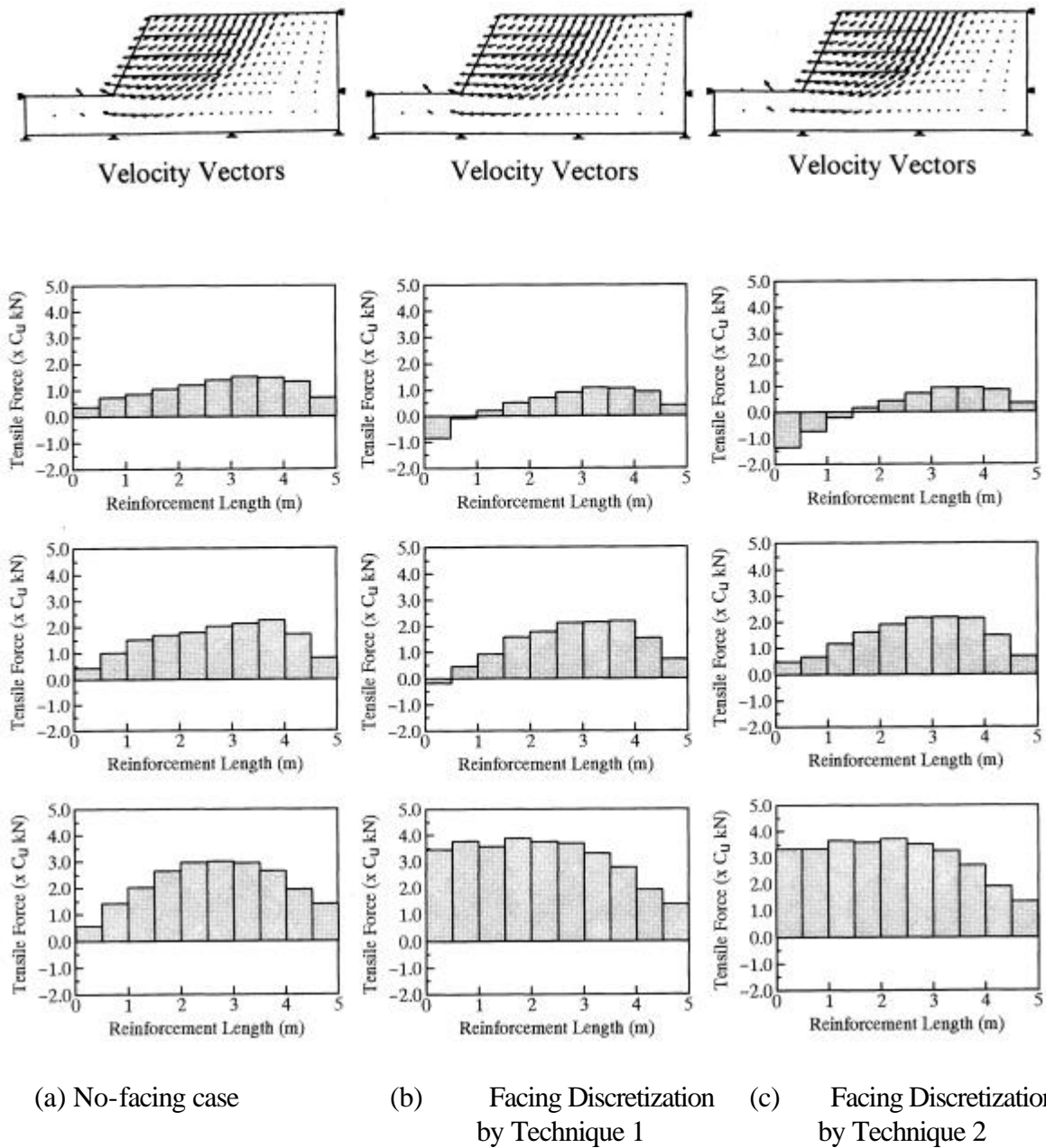


Figure 4.34 Effect of facings connected to multiple reinforcements on velocity field and the axial force distributions along reinforcements.

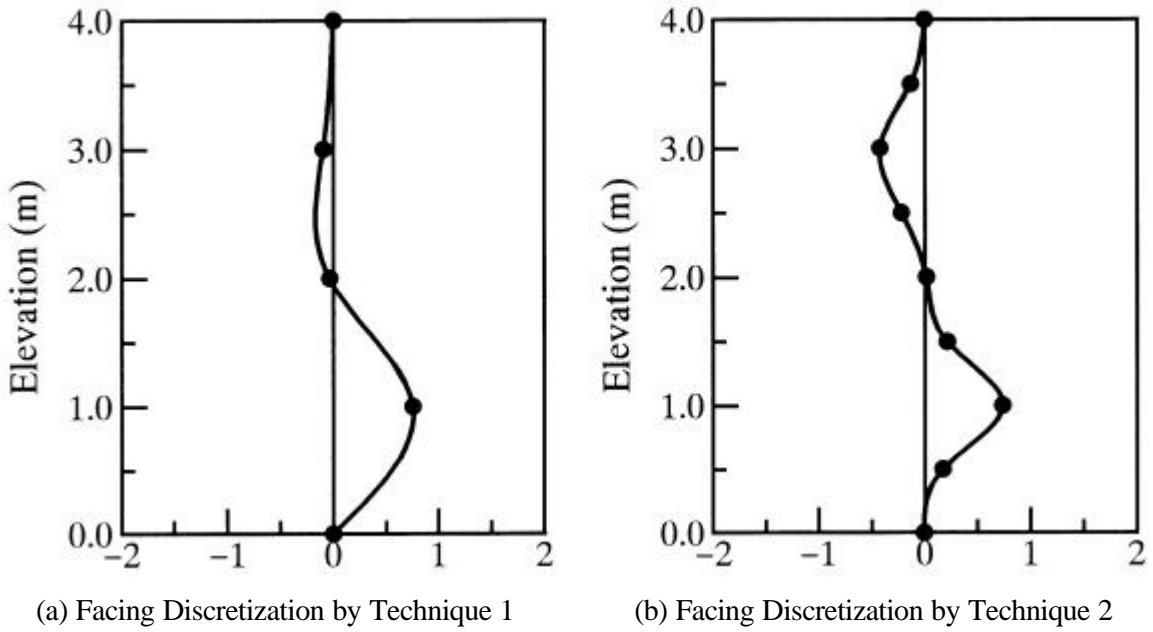


Figure 4.35 Computed bending moment distribution along the facing connected to a set of multiple reinforcements.

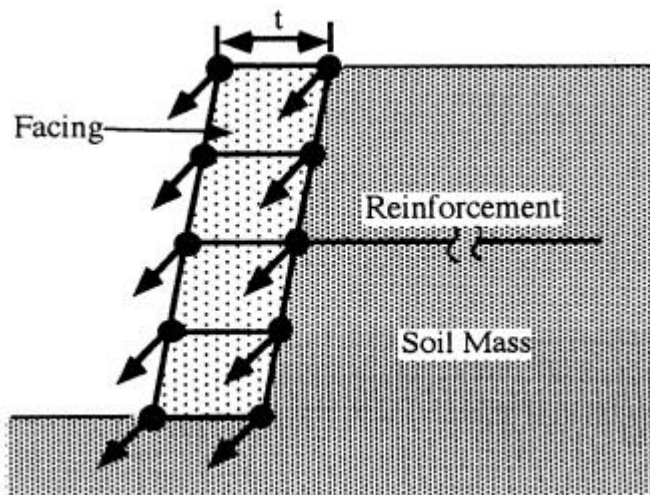


Figure 4.36 An alternative method of modeling the facing employing only the *no-length change* condition.

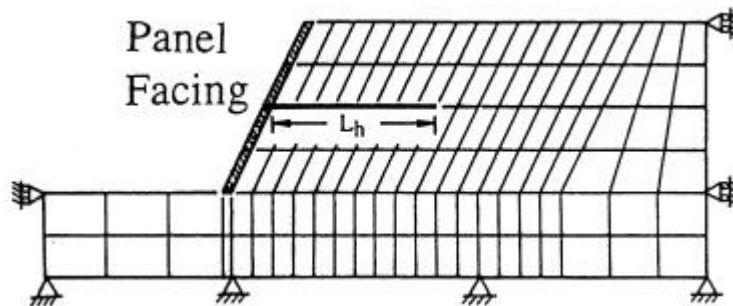


Figure 4.37 Finite Element Mesh used in the alternative method.

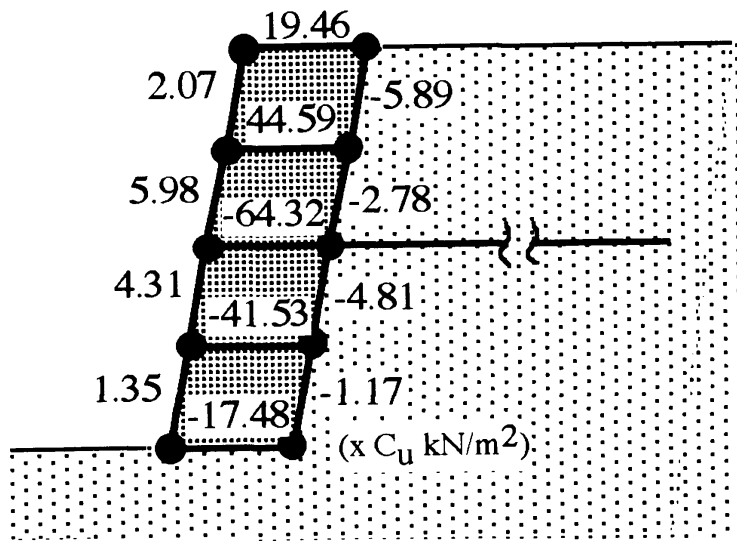
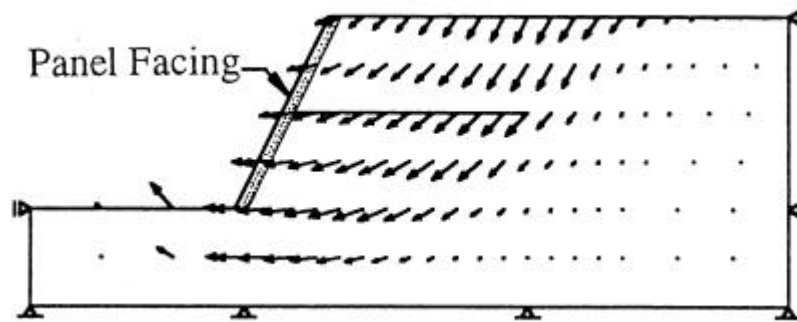
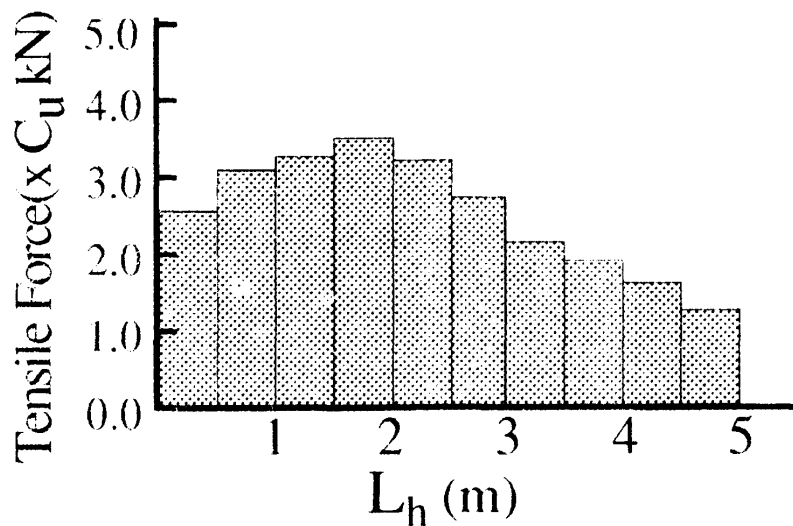


Figure 4.38 Tensile and compressive forces in the panel facing connected to facing.



(a) Velocity Vectors



(b) Tensile Force along the Reinforcement Length

Figure 4.39 Effect of the panel facing on velocity field and axial force distributions.

### 4.3.3 Sandy Soil ( $c$ - $f$ material)

The last representative problem taken is the stability analysis of a sandy slope (i.e. frictional,  $c$ - $f$ , material:  $c=4.4$  kPa,  $\phi=30^\circ$ ). As stated in the second chapter,  $c$ - $f$  material is analyzed as inhomogeneous Mises material satisfying the Mohr-Coulomb failure criteria at the limit state. The boundary conditions of the slope discussed in this example are shown in Fig. 4.40 that is similar to *Example 1* in this section concerning the slope face grading, thickness of the soil layer and the reinforcement positions. Two sets of analyses were carried out, first with single reinforcement and latter, with multiple reinforcements (Figs.4.41~4.44). Figure 4.41 shows the relationship of the computed factor of safety and the length of reinforcement in the former two cases. The reinforcing effect of the sandy ( $c$ - $\phi$ ) material is larger than that of the purely cohesive clay. Even a single short reinforcement produced the factor of safety as much as two times of the unreinforced soil (*see* Fig.4.45). Factor of safety considerably increases when soil is reinforced with multiple reinforcements, e.g., three reinforcements give about 5 times of the unreinforced slope.

Figure 4.42 shows the velocity field, the principal stress distributions and the mean confining stress distribution in the soil mass without reinforcement. The failure zones are very narrow and close to the slope face compared with the failure regions observed in the purely cohesive clay slope (Fig. 4.21).

The computed velocity fields, the principal stress distributions, the mean confining stress distributions and the tensile force distributions along the reinforcement are shown in Fig. 4.43 for a single reinforcement of varying lengths. For relatively short reinforcements, e.g. 1.5m, the widening effect of velocity field bears resemblance with the Mises material discussed in the earlier sub-section. Further increase in the reinforcement length divides the velocity field into two small zones on either side of the reinforcement as shown in Fig.4.43 (a). The inner end of the reinforcement also reaches rigid area ( $\bar{\epsilon} = 0$ , *see* Eq.3.40). The magnitude of the mean confining stress in soil mass around reinforcements shows a significant increase. The magnitude of the tensile force along reinforcements in such sandy soil mass is directly influenced by the magnitude of the mean confining pressure around the reinforcement. For the reinforcements approaching a high confining pressure zone, the tensile force magnitude increases substantially towards the zone (Fig. 4.43b). This behavior can be compared with an anchor used for rock bolting. Thus, the high confining stress in the sandy soil equivalently acts like a rock bolt.

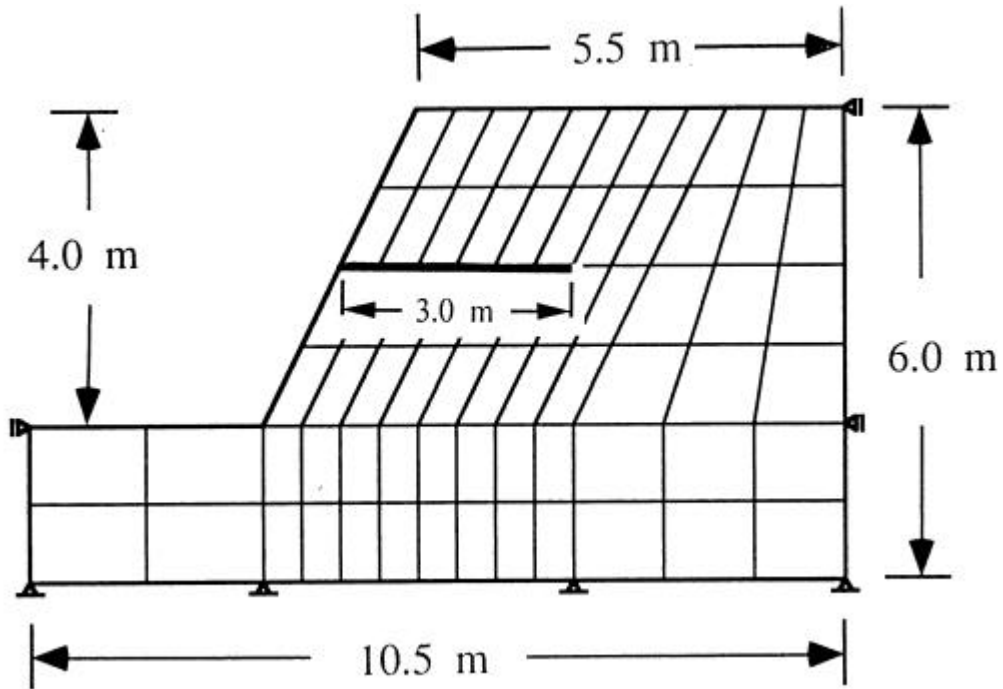


Figure 4.40 A typical finite element array for FE analysis of the reinforced slopes with frictional ( $c-\phi$ ) material.

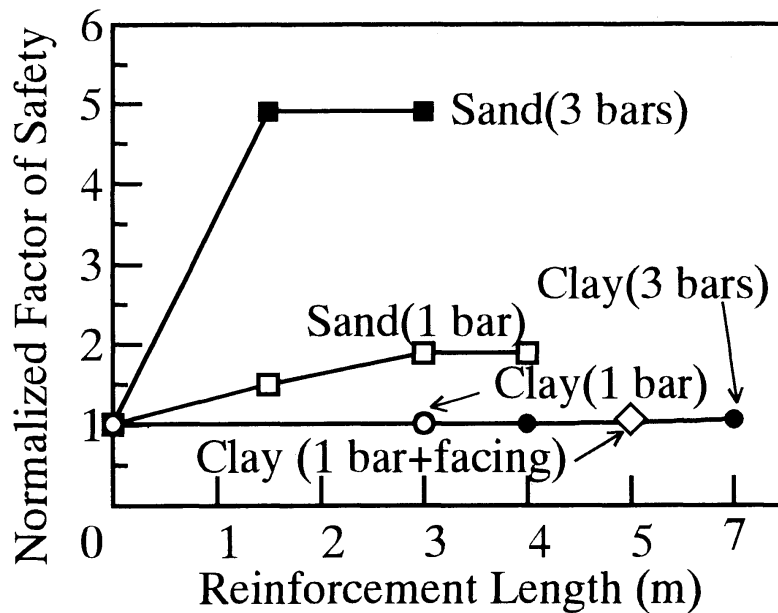
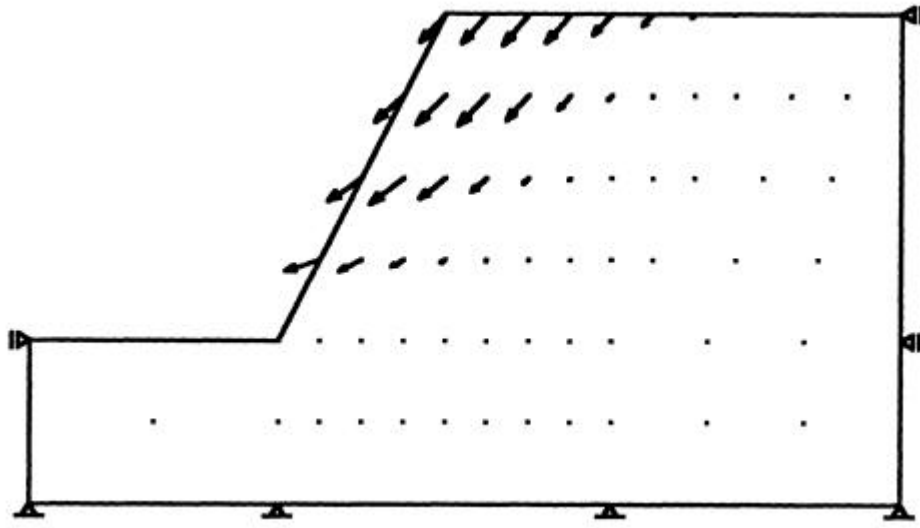
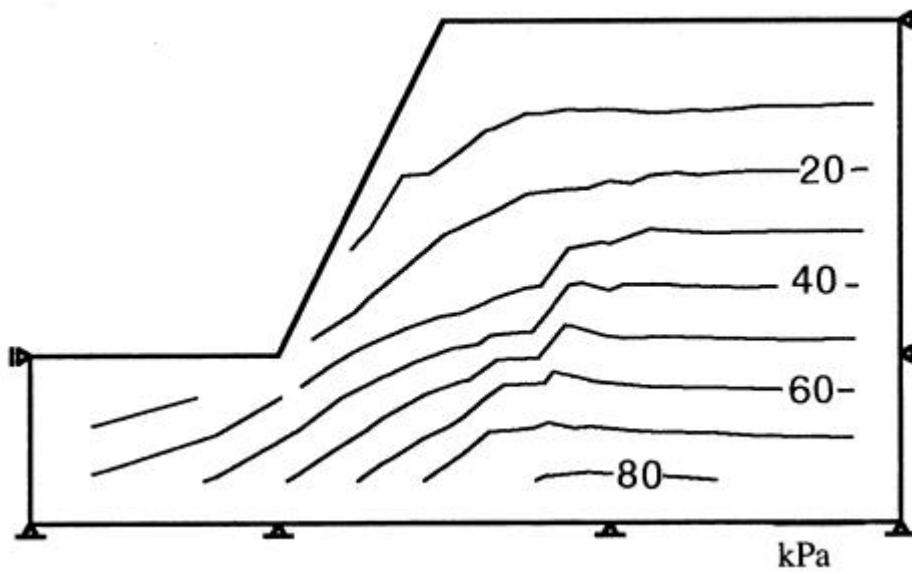


Figure 4.41 Computed factor of safety versus reinforcement length in a reinforced frictional soil and comparisons with the normalized safety factors for purely cohesive clay slopes.

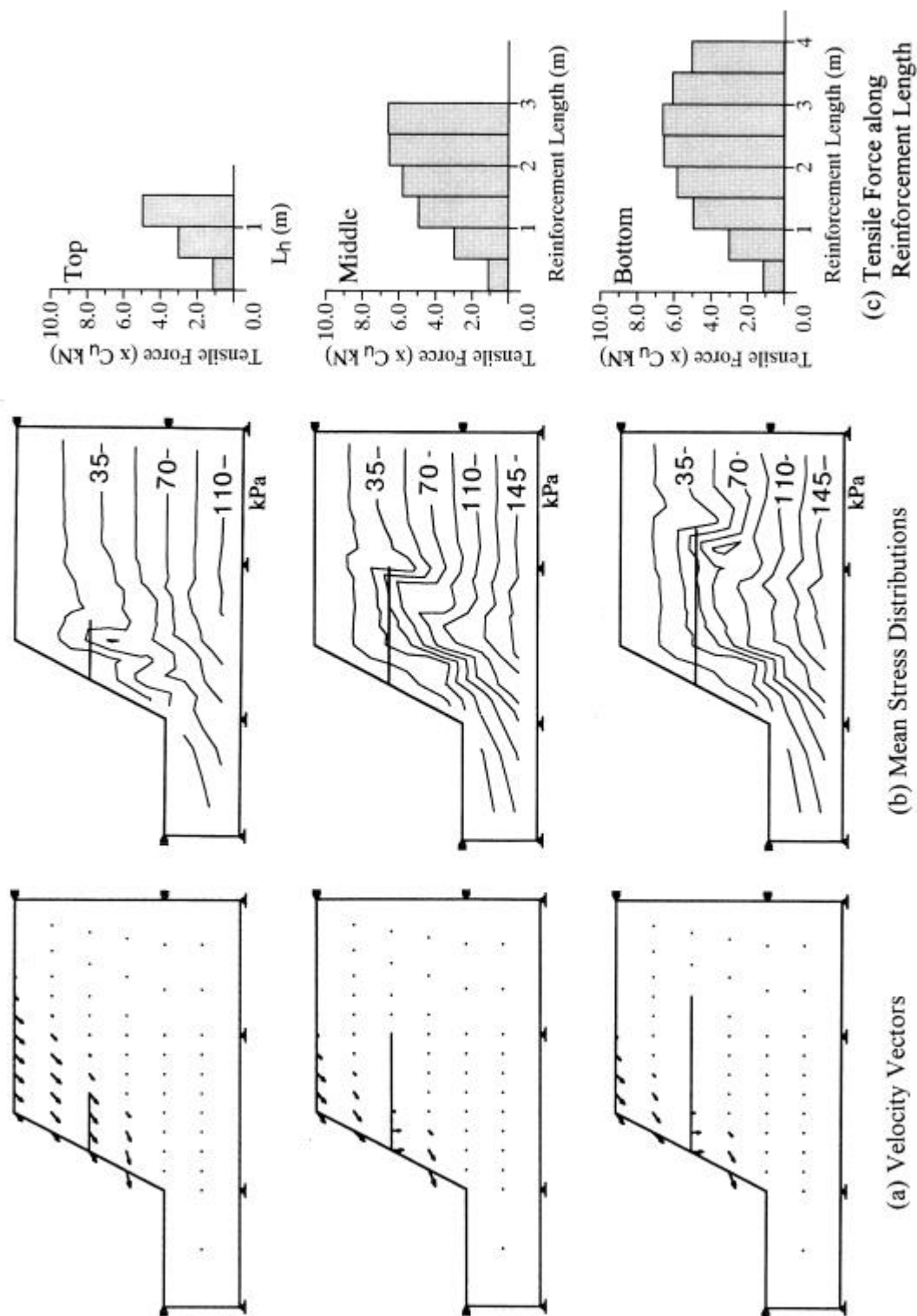


(a) Velocity Vectors



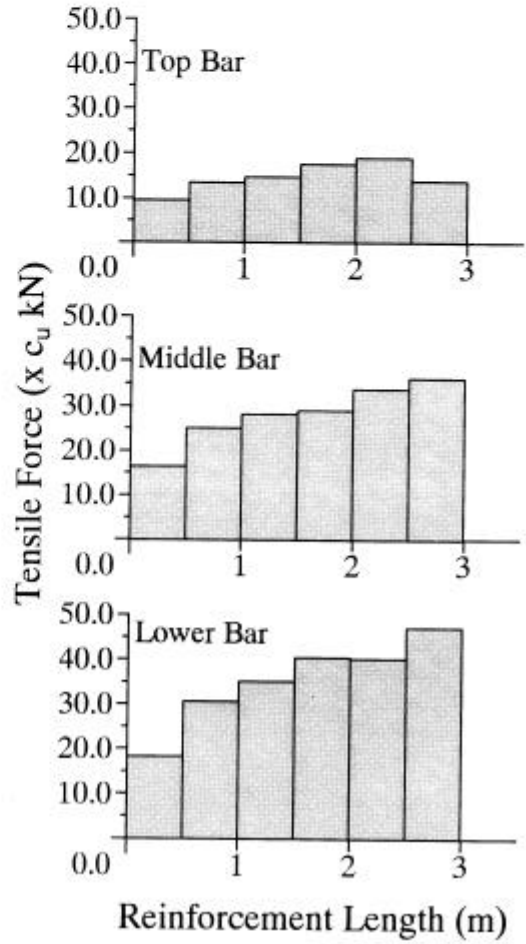
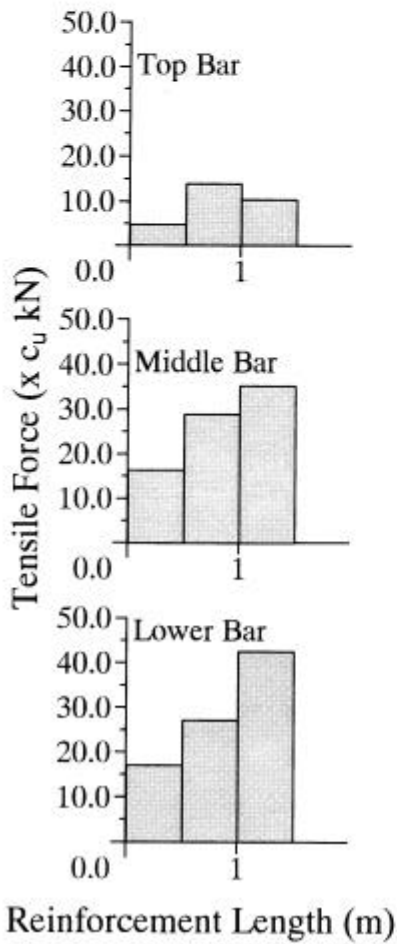
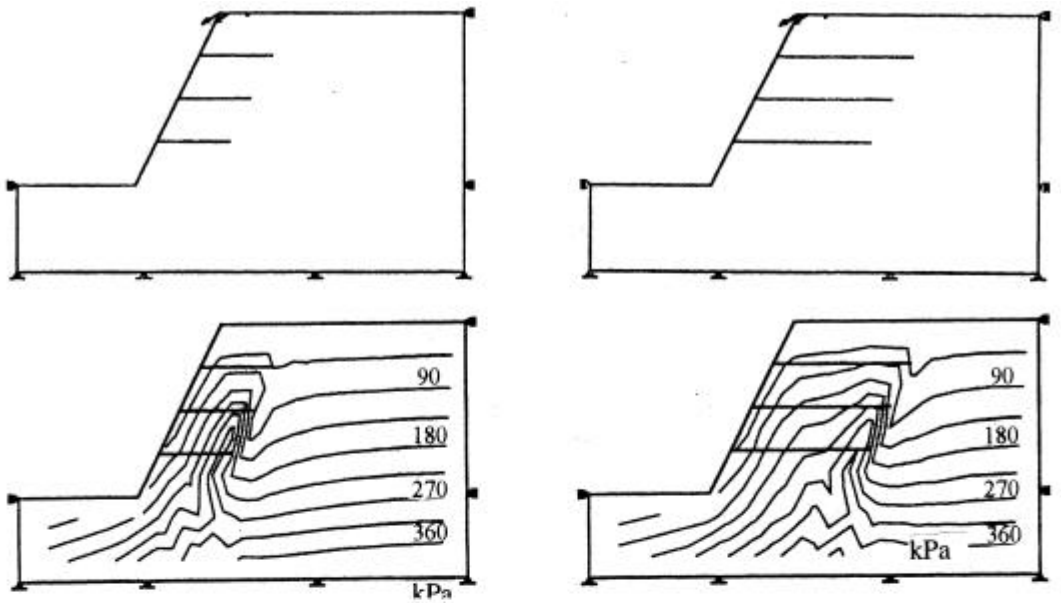
(b) Mean Stress Distributions

Figure 4.42 Velocity field, principal stress orientations and mean confining stress contours in a frictional soil ( $c-\phi$ ) without any reinforcing material.



(a) Velocity Vectors  
 (b) Mean Stress Distributions  
 (c) Tensile Force along Reinforcement Length

Figure 4.43 Velocity field, mean confining stress contours and axial force along reinforcements of different lengths in case of frictional soil ( $c-\phi$ ).



(a) Short Reinforcements (L=1.5m)

(b) Long Reinforcements (L=3.0 m)

Figure 4.44 Effect of multiple reinforcements on velocity field; mean confining stress contours and axial force distribution (*c-f* material).

#### 4.4 SUMMARY AND CONCLUDING REMARKS

---

The numerical method formulated in the previous chapter, Chapter III, by introducing a new concept of computation of bearing capacity/safety factor, distribution of the axial and the shear forces (/bending moment) in reinforcing members as well as velocity vectors and stress distribution in reinforced soil structures is investigated and the features/capability of the methodology is demonstrated through some typical reinforced soil engineering structures. The effects of tensile reinforcements and flexural materials are coupled in the conventional rigid plastic finite element method by introducing a set of constraint conditions of "*no-length change*" and "*no-bending condition*" of the soil element nodes corresponding to reinforcing members at the limit equilibrium state of the soil mass.

The proposed concept is tested numerically in one set of bearing capacity problems and two sets of slope stability problems with strip footing loading and gravity loading, respectively. The following conclusions are drawn through the present study:

1. The "*no-length change*" and "*no-bending*" conditions in the soil mass at the limit equilibrium state can be introduced in the plastic energy dissipation minimization problems. In this case, the Lagrange multipliers corresponding to the constraint condition of no-length change and no-bending condition represent respectively the axial force and the shear force in the reinforcing material per unit length.
2. In the bearing capacity problem of purely cohesive clay, a set of optimum reinforcement positions are obtained depending on the footing type. The maximum effect on the bearing capacity in the reinforced homogeneous clay mass is about 13% larger compared with the unreinforced case and 25% in the case of clay having linearly increasing shear strength with depth.
3. In the slope stability case, reinforcements have contrast effect on the safety factor of the problem depending on the soil type, i.e. purely cohesive clay or frictional ( $c-\phi$ ) material. The increase in safety factor in the frictional soil is quite higher than the purely cohesive clay due to the differences in the mechanism of reinforcements depending on the soil type. In frictional material, the bar acts like an anchor while in the purely cohesive clay the bar does not show such effects. Such effect was clearly explained through the velocity field, the mean confining pressure and the axial force distribution in the reinforcement.
- 4) For the first time, the effect of rigid panel facing is included in the stability analysis. The proposed method could explain well the effect of flexural rigidity of the facing. It can be explained with the axial and the shear force developed in the facing.